

Structural Design of the Rotor and Static Structure of a Microscale Rankine Engine

By
Hassan Shahriar



Department of Mechanical Engineering
McGill University
Montréal, Canada

Thesis submitted to McGill University in partial fulfillment of the requirements
for the degree of Master of Engineering

Under the supervision of:

Professor Srikar Vengallatore
Department of Mechanical Engineering
McGill University

© Hassan Shahriar
August 2009

Abstract

The goal of this thesis is to develop tools that will enable the design of the components of the Rankine micro-engine in order to satisfy performance and reliability requirements for high temperature operation. The Ashby approach was used to identify a set of candidate materials – zirconia, silica, titanium alloy, nickel-cobalt alloy, silicon carbide and silicon – for the insulating static structure and rotor. Subsequently, the stresses in, and deformations of, the insulating static structure were analyzed using analytical models and the method of finite elements.

Subsequently, an idealized impact experiment was designed and performed to assess reliability of the rotor in the event of an accidental high-speed impact with the static sidewalls. The threshold velocity for initiating damage in alumina projectiles (balls) impacting on alumina targets (discs) was found to be 30 m/s, while the corresponding value for zirconia projectiles on alumina target was found to be around 65–70 m/s. These findings pave the way for developing detailed designs for the rotor and static sidewall of the Rankine micro-engine.

Sommaire

L'objectif de cette thèse est de développer des outils qui permettront la conception de composants de moteur, afin de satisfaire les exigences de performance et de fiabilité de l'appareil dans des conditions extrêmes. La méthode Ashby a été utilisée pour identifier un ensemble de matériaux - la zircone, la silice, de l'alliage de titane, de l'alliage nickel-cobalt, de silicium et de carbure de silicium – pour la structure statique isolante du rotor, ce qui révèle un compromis entre la performance, la fiabilité et la fabricabilité . Ultérieurement, les contraintes, et les déformations de la structure statique d'isolation ont été analysées par la méthode des éléments finis.

Par la suite, une expérience idéalisée d'impact a été conçue et réalisée pour évaluer la fiabilité du rotor dans le cas d'un accident d'impact à grande vitesse avec la paroi latérale de la structure statique. La vitesse seuil d'ouverture des dommages dans des projectiles d'alumine (balles) un impact sur les objectifs de l'alumine (disques) a été retrouvé à 30 m/s, alors que le projectile en zircone sur la cible d'alumine a été jugé dans la région de 65 - 70 m/s. Ces résultats ouvrent la voie à la formulation de matériaux de conception pour le rotor et la paroi latérale statique du micro-moteur Rankine.

Acknowledgements

I would like to thank my supervisor, Prof. Srikar Vengallatore for guiding me through my Masters and for teaching me to be a better scholar and researcher. I extend my sincerest gratitude to the project collaborators, Prof. Luc Fréchette and Mokhtar Liamini, for their indispensable input towards my thesis.

I want to thank the great people of FDA 015 for bestowing on me the unique experience of meeting the world in a basement. Special thanks to Vahid Mirjalili, Guruprasad Sosale and Meysam Rahmat for having the patience to answer the myriad of questions to which they were regularly subjected to. I want to thank the ex-executive members of GAMES-McGill and the entire graduate community here at the department of Mechanical Engineering for making my Masters experience diverse and fulfilling.

Finally, I would like to thank my parents for their eternal support, Farzaneh for being the balance in my life and Edmon and Eve for being the great friends that they are.

This project would not have been possible without the financial support provided by the Natural Sciences and Engineering Council of Canada (NSERC) and General Motors of Canada (GMC).

Table of Contents

Abstract	ii
Sommaire	iii
Acknowledgements	iv
Table of Contents	v
List of Figures	viii
List of Tables	xiv
Chapter 1 - Introduction	1
1.1 Concept of Rankine cycle for harvesting waste heat	1
1.2 Advent of microscale heat engines	3
1.3 First generation Rankine micro-engine	4
1.4 Second generation Rankine micro-engine	5
1.5 Design Challenges	8
1.6 Goals and Structure of the Thesis	10
Chapter 2 – Preliminary Selection of Materials	11
2.1 The Ashby Approach	11
2.2 Length scale considerations	12
2.3 Identification of material indices	13

2.4 Material properties and selection chart	15
2.5 Summary	19
Chapter 3 – Analytical Models for Heat Transfer and Deformation.....	20
3.1 Thermal analysis of the static sidewall	20
3.2 Stress analysis for static sidewall.....	25
3.2.1 Euler-Bernoulli beam analysis	26
3.2.2 Plane strain elasticity	31
3.2.2.1 Stress due to internal pressure	31
3.2.2.2 Stress due to temperature difference	33
3.2.3 Shell Theory	37
3.3 Summary of analyses	49
Chapter 4 – Finite element analysis.....	50
4.1 Summary	56
Chapter 5 – Experimental Studies of Particle-Plate Impact	57
5.1 Background	58
5.2 Goal of the experiment.....	59
5.3 Design of experiment	59
5.4 Velocity estimation and verification	67
5.5 Particle impact experiment: Test materials and results.....	70
5.5.1 Results – Alumina spheres on alumina disc.....	71

5.5.2 Results – Zirconia spheres on borosilicate glass.....	74
5.5.3 Results – Zirconia spheres on alumina.....	75
5.6 Summary.....	78
Chapter 6 – Conclusions and Future Work	79
References.....	82

List of Figures

- Figure 1-1:** Schematic of a typical Rankine cycle used to transform heat to electricity. (Source: D. Lindley, Nature, vol. 458, pp. 138-141 (2009)) 2
- Figure 1-2:** (a) Exploded view of the first generation Rankine micro-engine. The bottom four layers are etched silicon and the top layer is glass. The microfabricated rotor is indicated. (b) Scanning electron micrograph of the microfabricated rotor of diameter 4 mm showing four concentric rotor blade stages. (Source: M. Liamini, U. Sherbrooke) 4
- Figure 1-3:** Schematic illustration of the multi-spool configuration of four Rankine Microturbines. Turbine 4 also incorporates the pump. Arrows show the path of the working fluid and their approximate temperatures. 6
- Figure 1-4:** Schematic cross-section of a Rankine Microturbine: (1) rotor, (2) thrust bearing, (3) journal bearing, (4) evaporator, (5) condenser, (6) insulating sidewall, (7) pump, and (8) generator. The structure is ~1 mm in thickness and ~10 mm in diameter. 7
- Figure 1-5:** Schematic cross-section of the static structure and rotor. The static structure consists of upper and lower plates, and a cylindrical sidewall. The black arrows represent heat leakages through the side wall and P is the internal pressure. 8
- Figure 2-1:** (a) Vertical section of the static sidewall showing heat leakage through the structure with r_i as the inner radius. Arrows indicate heat leakages. (b) Horizontal section of the static wall showing P as the internal pressure in the chamber..... 13
- Figure 2-2:** Material selection chart based on material properties obtained from published literature over a wide range of temperature. The oxides include zirconia (stabilized), silica, quartz and titania; the alloys are titanium alloy VT6 and nickel-cobalt alloy; and the ceramics are silicon and silicon carbide. The vertical axis represent the first material index, and the red dashed lines represent the second material index. 18

Figure 3-1: Cross-sectional area of the static sidewall surrounding the rotor. (a) Top view of the maximum possible area of the wall for the entire chip. (b) Top view of a cylindrical wall of thickness t 22

Figure 3-2: Thermal efficiencies of the Rankine micro-engine for a power output of ~ 8 W. The curves represent the variation of thermal efficiencies as a function of thermal conductivity for two area configurations. Arrows show the range of efficiencies that can be obtained using different materials. The values indicated correspond to thermal conductivities at 773 K. 23

Figure 3-3: Range of annular wall thicknesses for different materials generating device efficiency of at least 10%. Silica and zirconia has a larger thickness range compared to silicon and silicon carbide. 24

Figure 3-4: The static sidewall (not to scale). (a) Vertical section of the static sidewall bonded to the evaporator and condenser. (b) Vertical section showing sidewall thickness t and its length L . (c) Horizontal section showing the inner radius r_i and outer radius r_o . (d) A 3D view of the static wall. 26

Figure 3-5: Differential element (rectangular orange) of the sidewall assumed to be a beam. 27

Figure 3-6: (a) Axial differential element of the sidewall assumed as a clamped-clamped beam with a distributed load of P_o . (b) Free-body diagram of the clamped-clamped beam..... 28

Figure 3-7: Variation of stress as a function of the thickness-to-length ratio, ψ , for zirconia. For a fixed wall length, the stress due to internal pressure dominates for thinner sidewall, and the stress due to deflected end dominates for thicker walls. 29

Figure 3-8: Design space for static sidewall thickness for selected ceramics, alloys and oxides. The bars on the left indicate thickness range satisfying 10% efficiency, and those on the right indicate thickness ensuring reliability for an internal pressure of 1 MPa..... 30

Figure 3-9: Schematic of the static sidewall for the 2D plane strain analysis. P_o is the internal pressure. r_i and r_o are the inner and outer radii respectively. The ambient pressure (atmospheric) is considered much smaller than the internal chamber pressure and is thus neglected. 32

Figure 3-10: Dimensionless thermal stress variation for the three stress components in the radial direction as a function of dimensionless radii. Maximum stresses occur on the inner surface.	35
Figure 3-12: Dimensionless circumferential stresses as a function of the ratio of radii for the static sidewall. The dimensionless mechanical stress is higher than the dimensionless thermal stress for smaller ratios (thinner sidewall). 36	
Figure 3-12: (a) A shell element with radii of curvature R_α and R_β much larger than the thickness h . (b) The stress resultants per unit length obtained by integrating out the thickness. (c) Kirchoff's hypothesis of straight normals, a critical assumption in the shell theory. (d) A section of the curved surface indicating the estimation of the stresses of a plane ζ distance from the middle surface.	38
Figure 3-13: (a) Vertical section of the sidewall with thickness h . (b) The stress and moment resultants of the neutral.	39
Figure 3-14: Solid lines represent the stresses on the inner surface of the sidewall. Thickness is taken to be 200 μm and the internal pressure is 5 MPa. The dash-dot-dash lines represent the hoop and the longitudinal stresses for a long pressure vessel obtained from plane-strain elasticity.	44
Figure 3-15: Stress components for various lengths of the annular cylinder: (A) 10 mm cylinder; (B) 5 mm cylinder; (C) 2 mm cylinder; and (D) 0.5 mm cylinder.	45
Figure 3-16: Differential element of the static sidewall with respective temperatures on the various surfaces.	46
Figure 3-17: Variation of stress components along the length of the pressure vessel subjected to a thermal field ($T_h = 500^\circ\text{C}$, $T_c = 80^\circ\text{C}$ and $T_{\text{ref}} = 25^\circ\text{C}$) and an internal pressure of 5MPa. The solid lines represent stresses of the inner wall. The dashed lines represent stresses of the outer wall. Blue, green and red represent axial, circumferential and shear stresses respectively.	47
Figure 4-1: Principal stresses for static sidewall on elastic foundations obtained through FEA. The inset on the upper right hand corner shows the stresses obtained using shell theory for clamed edge boundary conditions. The inset on the upper left corner shows the result of the finite element analysis.	51

Figure 4-2: Axisymmetric schematic of the static structure modeled as a pressure vessel outlining structural dimensions, materials and the applied boundary conditions.	52
Figure 4-3: Modified schematic of the static structure including a radial extension outside the pressure chamber. Fillets are applied at all the corners where the inner and outer walls meet the upper and lower surfaces.	53
Figure 4-4: Variation of the maximum principle stress as a function of fillet radii obtained through a static finite element analysis. The solid lines represent the edge stresses of the inner and outer walls for a static structure of 5 mm radius. The dash-dot lines represent the change in edge stresses for a static structure of 3 mm.	54
Figure 4-5: Results of the coupled thermo-mechanical finite element analysis with a static structure extension of 1 mm. The maximum stress for the outer wall is 140 MPa and is compressive. The location of the maximum deflection is indicated by the arrow and is approximately 0.69 μm	55
Figure 5-1: Threshold velocity plot for silicon nitride and alumina impacting on titanium diboride. (Source: E. W. Andrews and K. S. Kim (1998) <i>Mechanics of Materials</i> , vol 29: pp. 161-180).	58
Figure 5-2: Schematic for particle impact experiment setup. (Source: E. W. Andrews and K. S. Kim (1998) <i>Mechanics of Materials</i> vol. 29, pp. 161-180).	60
Figure 5-3: (a) Schematic of sample-sabot-barrel system (image not to scale). (b) Free body diagram of the sample and the sabot.	61
Figure 5-4: Design curve of the barrel length and bore diameter for the gun barrel for $V = 100 \text{ ms}^{-1}$, $P_0 = 7 \text{ bars}$ and $m = 0.005 \text{ kg}$	62
Figure 5-5: Schematic of the piping system for the gas gun system. The compressor includes a regulator, a pressure gauge and an air tank.	65
Figure 5-6: Particle impact experiment setup. (1) Target holder (2) Ruler (3) Protective casing (4) End cap (5) Barrel (6) Solenoid valve (7) Ball valve (8) Air tank (9) High speed camera (10) Lamp (11) Trigger switch (12) Support structure (13) Pressure gauge (14) Ball valve (15) Air compressor.	66

Figure 5-7: (a) Two frames of the particle trajectory for a 5psi (34kPa) air tank pressure. The frames are 0.0025 seconds apart. (b) Extracted frames for a 50psi (344kPa) air tank pressure. The frames are 0.000833 seconds apart. Due to lack of luminous intensity, the particles appear as a blur, more so for higher velocities. 67

Figure 5-8: The solid black line represents the calculated velocity of the particle based on equation 5.1 where the parameters d , D_s , m and P_o are known. The red and the blue points represent the estimated velocities of the particle based on the extracted frames from the movie of the particle trajectory. 68

Figure 5-9: Particle fired with an air tank pressure of 70 psi (483kPa). The white arrow indicated the location of the spherical particle in three consecutive frames. Image source: High Speed video camera model MS50K with high illuminance light source – Optikon Corporation..... 69

Figure 5-10: (a) Three consecutive frames of capturing the fragmentation of the alumina ball. Arrow in the first frame shows the direction of the ball. Arrows in the third frame shows the direction of the ball fragments (b) Post impact remains of the alumina balls (impact velocities indicated)..... 72

Figure 5-11: Calculated and experimental velocities of the alumina ball impacting on alumina target. Filled circles indicate fragmentation of the alumina particle, while hollow circles indicate rebound..... 73

Figure 5-12: Damage of borosilicate glass at various impact speeds with zirconia spheres. Cone cracks appear at lower velocities. At 39 m/s, a conical piece is removed from the target. Frosted regions and lateral cracks appear at higher impact velocities. 74

Figure 5-13: Scanning electron micrograph of borosilicate glass after impact at (a) 23 m/s, and at (b) 69 m/s. Images show material removed from the impacted region..... 75

Figure 5-14: Calculated and experimental velocities of the zirconia balls impacting on alumina target. Filled circles indicate fragmentation of the zirconia ball, while hollow circles indicate rebound. The partially filled circles represent ball samples that remained intact but possessed visible surface cracks..... 76

Figure 5-15: Scanning electron micrograph of a zirconia ball after impact at 69.5 m/s. A ring crack forms in the contact zone together with lateral cracks extending across the ball surface. 77

Figure 5-16: Split pieces of a zirconia ball formed through lateral separation mode..... 77

List of Tables

Table 2-1: Thermal conductivity (W/m/K) of selected oxides, ceramics and alloys at elevated temperatures 298K – 673K.....	16
Table 2-2: Thermal conductivity (W/m/K) of selected oxides, ceramics and alloys at elevated temperatures 298K – 673K.....	16
Table 2-3: Ranges for flexural strength (MPa) of selected oxides and ceramics at elevated temperatures.....	17
Table 2-4: Yield Strength (MPa) of selected alloys.....	17
Table 3-1: Summary of the analytical models undertaken in this chapter	49
Table 5-1: Materials, shapes and sizes used in the particle impact experiment...	70
Table 5-2: Selected properties of test materials	71

Chapter 1 - Introduction

In an age where portable electronic devices are ubiquitous, there is a clear and distinct need for new types of compact power supply, as opposed to chemistry-based batteries. Such power systems are being realized with the advent of microfabrication techniques [1]. These power generating systems are typically millimetre-sized devices and are designed to deliver power ranging from 100 μ W to 10 W, depending on the application. The various concepts currently being explored are miniaturized heat engines, fuel cells, thermoelectric and thermophotovoltaic devices, and vibration energy harvesters. Of particular interest to this thesis are the heat engines, specifically a heat engine operating a Rankine cycle.

1.1 Concept of Rankine cycle for harvesting waste heat

The Rankine cycle – named after William Rankine, a nineteenth century Scottish engineer – is typically used to generate electricity in power plants. Using water as the working fluid, this cycle is able to generate mechanical power from a given temperature difference. In a typical power plant (Figure 1-1), water is pumped in to a boiler, where it is vaporized to form high pressure steam. The steam is then expanded through a turbine whose rotating shaft produces power in the generator. The steam is condensed back into water in a condenser and is then pumped back into the boiler. The temperature-entropy diagram for this cycle

indicates that the power output and efficiency can be increased by increasing the temperature difference between the boiler (evaporator) and condenser.

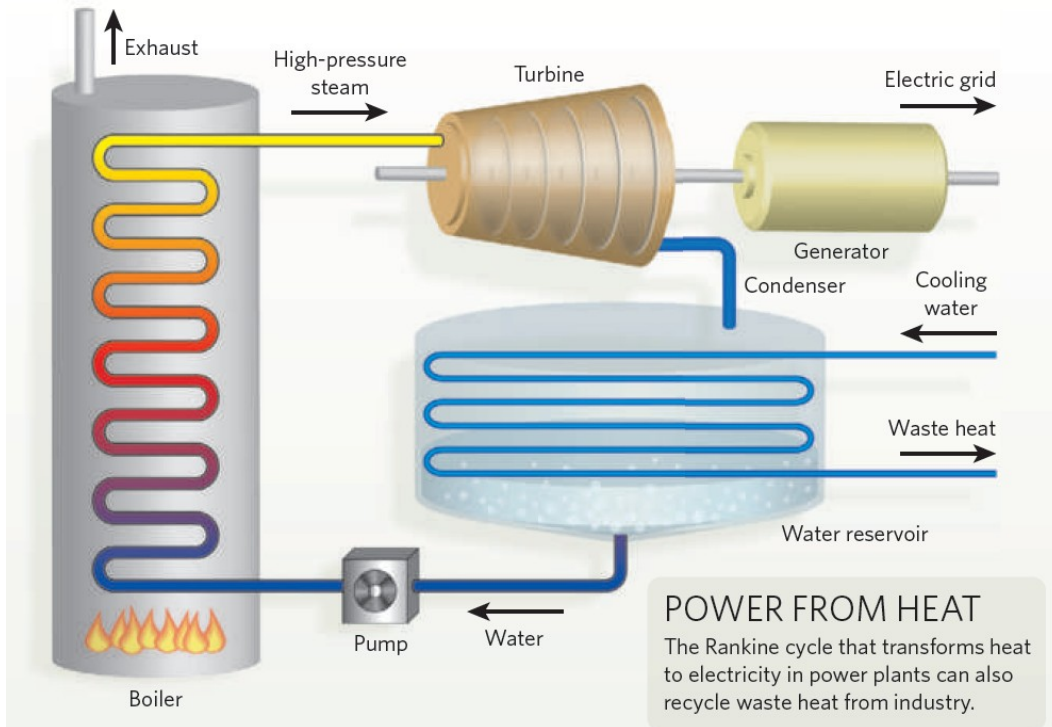


Figure 1-1: Schematic of a typical Rankine cycle used to transform heat to electricity. (Source: D. Lindley, *Nature*, vol. 458, pp. 138-141 (2009))

The Rankine cycle uses a closed loop system whereby the working fluid is continuously reused as it is transformed between the liquid and vapour phases. This closed loop operation enables the system to use various heat sources as long as the working fluid is able to achieve two-phase flow between the heat exchangers. Owing to the flexibility of heat sources, Rankine cycles are also used as a bottoming cycle for large industrial plants, such as ore-smelting and metal-refining plants [2], where the typical exhaust temperature from the kilns average around 800 °C. In doing so, these plants can recover part of the waste heat being

emitted into the atmosphere, which translates to large cost savings for these industrial plants. Following the same train of thought, one can imagine using micromachining technology to build millimetre-scale devices that employ the Rankine cycle. These miniaturized engines can then act as waste heat energy harvesters to power microscale sensors and actuators used in automobiles and industries.

1.2 Advent of microscale heat engines

The first attempt to apply the techniques of microfabrication and microelectromechanical systems (MEMS) to heat engines dates back to 1994, when a group at MIT attempted to build a millimetre-scale gas turbine engine [3]. This decade-long effort generated a rich set of techniques and knowledge, thus motivating the development of other types of miniaturized engines for portable power generation and energy harvesting.

In 2003, Fréchette and his students (first at Columbia University, now at Université de Sherbrooke) initiated the effort to develop a microscale Rankine engine.

1.3 First generation Rankine micro-engine

The first generation Rankine micro-engine was developed in order to demonstrate the multistage silicon microturbine [5]. The device (Figure 1-2) consisted of four layers of shallow and deep reactive ion etched silicon, and one layer of an ultrasonically drilled Pyrex glass. These wafers were assembled together using anodic and fusion bonding. A 4 mm diameter microfabricated rotor was placed within this assembled structure, and was spun on thrust (air) bearings at speeds approaching 330,000 revolutions per minute (RPM) at ambient temperature. Later the core microturbopump was demonstrated and characterized [6]. The viscous pump was demonstrated experimentally and could pressure up to 240 kPa and thus deliver a maximum flow rate of 9 mg/s.

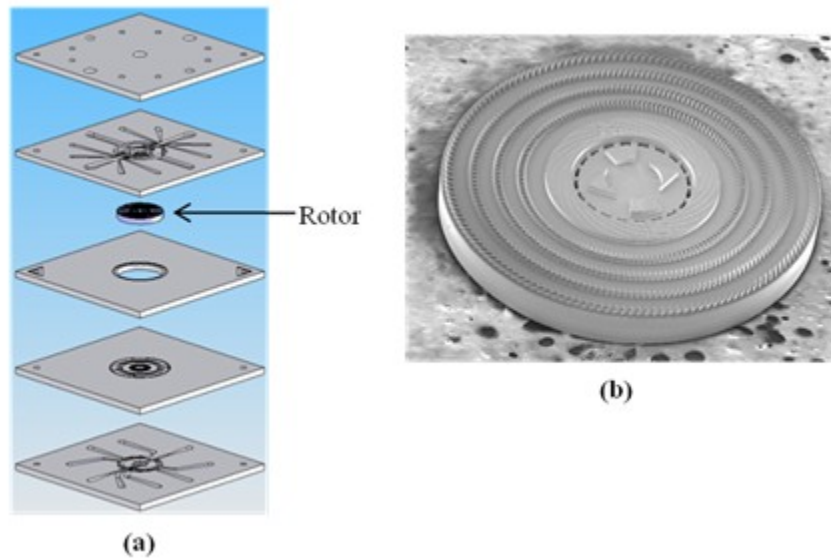


Figure 1-2: (a) Exploded view of the first generation Rankine micro-engine. The bottom four layers are etched silicon and the top layer is glass. The microfabricated rotor is indicated. (b) Scanning electron micrograph of the microfabricated rotor of diameter 4 mm showing four concentric rotor blade stages. (Source: M. Liamini, U. Sherbrooke)

1.4 Second generation Rankine micro-engine

The success of the first generation Rankine micro-engine motivated a collaboration between McGill University and Université de Sherbrooke to develop the next generation of Rankine micro-engines. The goal of the second generation Rankine micro-engine is to demonstrate operation using a two-phase working fluid (water and steam) at temperatures on the order of a few hundred degrees centigrade. This implies that the second generation device will experience temperature gradients of several hundred degrees centigrade per millimetre. A proposed multi-spool engine configuration consisting of four Rankine Microturbines arranged in series is illustrated in Figure 1-3. The first three stages (denoted Turbines 1, 2 and 3) are used for electric power generation. Turbine 4 is exposed to lower temperature steam and drives the pump. The total electric power produced by this configuration is estimated to be about 26 W, assuming that the turbines driving the generators rotate at 1.2 million rpm, and the turbine driving the pump rotates at 600,000 rpm [7].

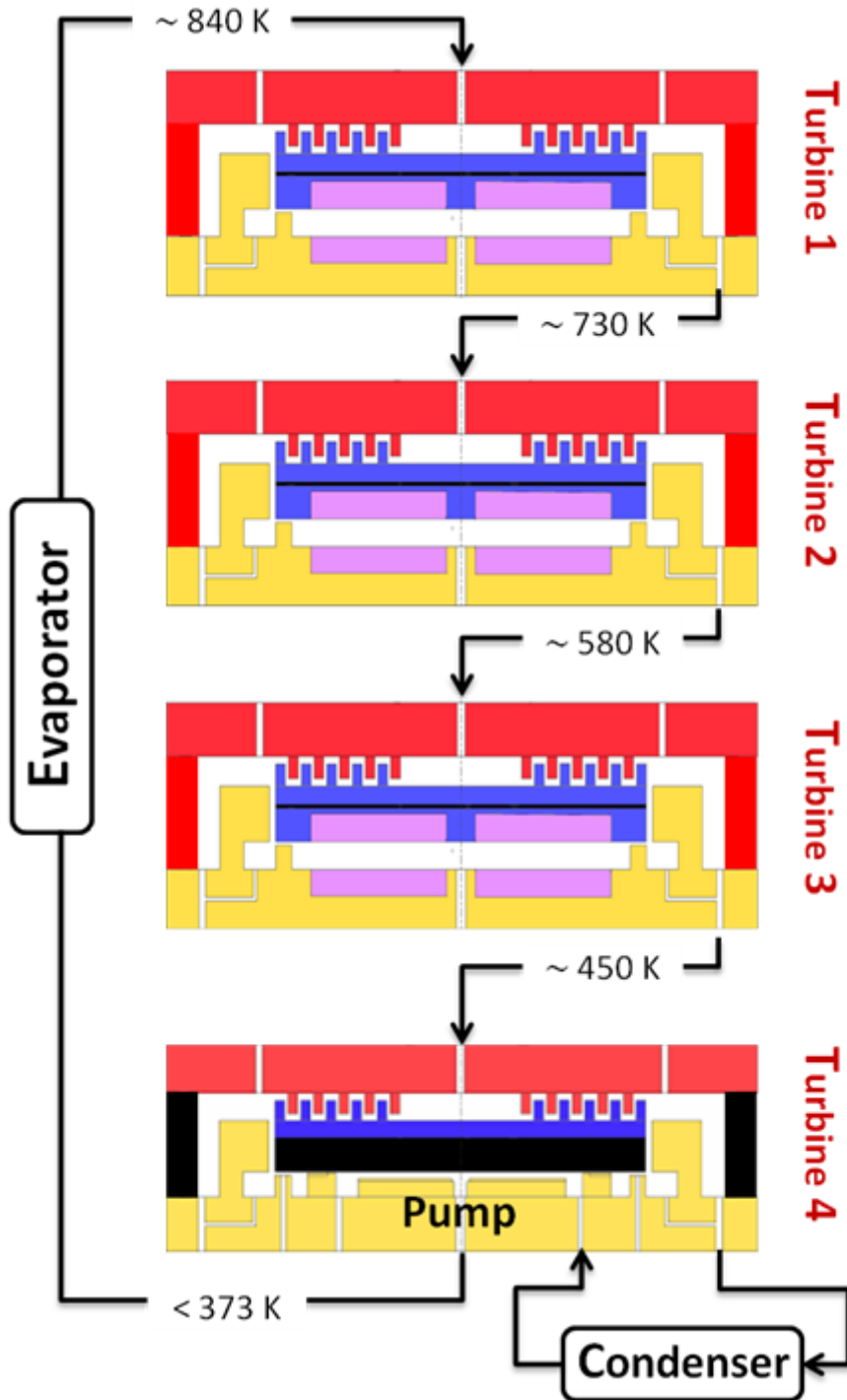


Figure 1-3: Schematic illustration of the multi-spool configuration of four Rankine Microturbines. Turbine 4 also incorporates the pump. Arrows show the path of the working fluid and their approximate temperatures.

A comparison of the four turbines reveals that Turbine 4 embodies within itself all the major design challenges in terms of high-speed rotating components, fluid management, thermal insulation, and structural integrity. A schematic cross-section of this device is shown in Figure 1-4.

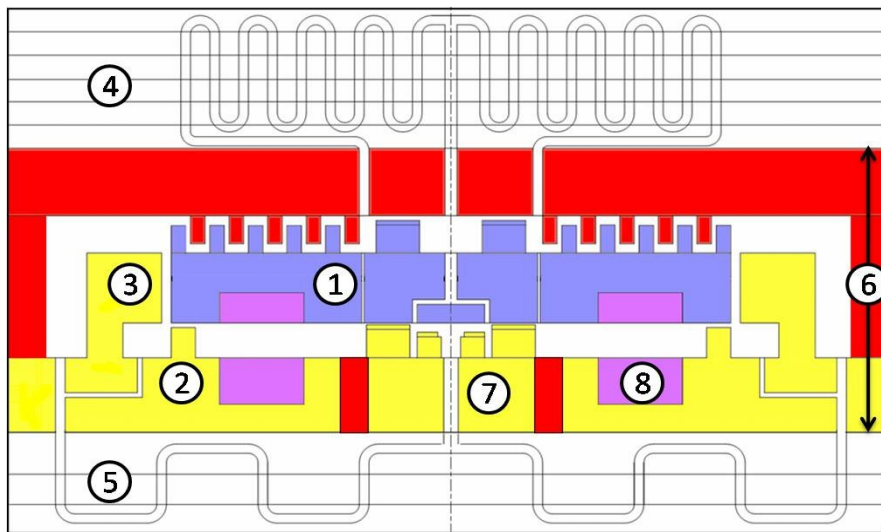


Figure 1-4: Schematic cross-section of a Rankine Microturbine: (1) rotor, (2) thrust bearing, (3) journal bearing, (4) evaporator, (5) condenser, (6) insulating sidewall, (7) pump, and (8) generator. The structure is ~1 mm in thickness and ~10 mm in diameter.

The rotor (1) is held in place by thrust bearings (2) and a journal bearing (3). The evaporator (4) is separated from the condenser (5) by a static insulator (6). The pump (7) is located underneath the rotor, and generators (8) are integrated into the stationary and rotating structures to generate electricity. The device is ~1 cm in diameter and ~1 mm in thickness.

1.5 Design Challenges

At this stage, it is important to highlight the operating conditions which Turbine 4 is expected to experience. Figure 1-5 shows a schematic cross-section of the static structure, which consists of two plates and a sidewall. The upper and lower plates are maintained at different temperatures during operation because they are in contact with the (hot) evaporator and (cold) condenser, respectively.

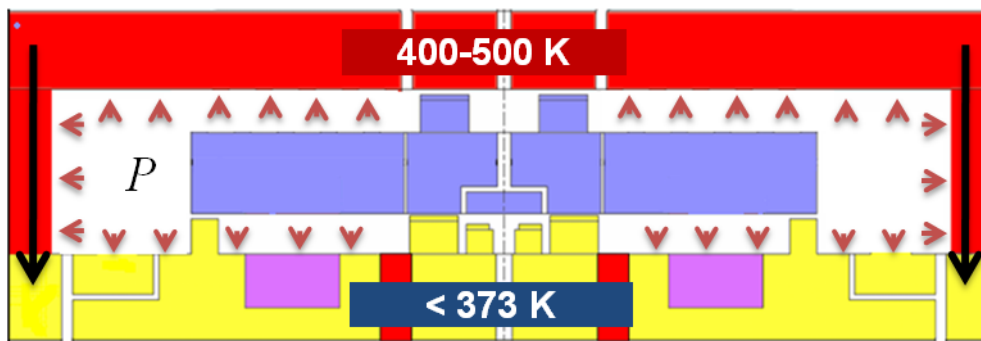


Figure 1-5: Schematic cross-section of the static structure and rotor. The static structure consists of upper and lower plates, and a cylindrical sidewall. The black arrows represent heat leakages through the side wall and P is the internal pressure.

For automotive applications, this temperature difference ranges from 150 K to 700 K; the lower end is the value that is generally recognized as the minimum useful temperature difference for the Rankine cycle, and the upper bound corresponds to the maximum temperature difference between the exhaust gases and the ambient. In this thesis, we shall consider the hot surface to be above 500 K and the cold surface to be below 373 K (to prevent vaporization at the pump). To generate power at the desired level of a few Watts, an internal pressure of ~ 3 MPa, and rotor speeds between 0.5 and 1.0 million rpm, are needed [8]. These operating conditions (fluidic pressure, differential thermal expansion, and

high spin speeds) generate both mechanical and thermomechanical stresses within the static structure and the rotor. The high temperature gradient between the hot and the cold surface promotes heat leakage through the static sidewall and adversely affects device efficiency. In addition, the deformation due to thermal expansion and fluidic pressure can lead to distortions of the static structure. This, in turn, can engender undesirable changes of critical gaps, such as those of the seals and thrust bearings.

The Rankine micro-engine occupies a design space that contains new combinations of materials, dimensions, layout, and operating conditions that have never been explored. Therefore, there is a critical need for developing a robust methodology for guiding the design of this micro-device.

1.6 Goals and Structure of the Thesis

The aim of this thesis is to develop approaches and tools that will guide the structural design of the second generation Rankine micro-engine. To achieve this aim, two goals were formulated: (i) develop approaches for the selection of materials and shapes for the engine components, and (ii) assess the dynamic reliability of the rotor in the event of accidental impact with the static sidewalls.

The progress made towards the first goal is described in Chapters 2, 3, and 4. The approach adopted is to make an initial selection of materials using the Ashby approach. Following this, analytical models of increasing complexity are implemented for heat transfer and mechanical deformation, with the aim of understanding the effects of material properties and geometry on the performance and reliability of the device. Finally, a coupled thermo-mechanical finite element analysis (FEA) of one specific design of the device is undertaken. Design modifications are proposed and analyzed to address concerns identified during finite element analysis.

Chapter 5 describes the progress made towards the second goal by considering the idealized case of high-speed impact of brittle particles on brittle targets. The literature on this phenomenon is sparse, and it was therefore necessary to design and instrument an experiment to study impact. The results of these experiments provide some guidelines for the structural design of the rotor.

Chapter 6 presents the principal conclusions of this thesis, and identifies areas for future studies.

Chapter 2 – Preliminary Selection of Materials

The materials used for the components of the Rankine micro-engine must enable high device performance, ensure sufficient reliability, and be compatible with the limitations imposed by state-of-the-art microfabrication techniques. The selection of appropriate materials is therefore crucial for the viability of the device. The first step is to derive material indices, using the Ashby approach, which directly affects the performance of the device. A set of materials which maximizes performance is then selected, as described below.

2.1 The Ashby Approach

The *Ashby Approach* [9] is a well known approach to material selection, enabling designers to identify materials best suited for specific functions of a component being designed. This approach to material selection for a particular component involves defining a performance function p of the form

$$p = p_1(F)p_2(G)p_3(M). \quad (2.1)$$

Here F, G and M represent the functional requirements, the geometric parameters and the material indices, respectively. The Ashby approach can be implemented in a step-by-step approach as follows: identify the **objectives and constraints** of the

given component; formulate equations for the objective and constraints while **eliminating the free variables**; isolate the **material indices** from those given equations; construct **materials charts** in order to identify suitable materials for ranking; and select **prime candidates**.

While this approach has been developed for macroscopic design process, it is also useful for the preliminary selection of materials for MEMS design [10] – as long as scale-dependent material properties are taken into account.

2.2 Length scale considerations

The effect of size and processing techniques on the material properties of macroscale and microscale structures has been studied intensely for several decades. Material properties whose physical origins lie at the atomic scale can be considered to be the same for micro ($>1\mu\text{m}$) and bulk (macroscale) structures [10]. These properties include the Young's modulus, Poisson's ratio, density, coefficient of linear expansion, and specific heat per unit mass. On the other hand, properties such as fracture strength and yield strength have values that can vary by orders of magnitude over different length scales. Typically, strength values increase as size decreases due to the reduced probability of critical defects and increased constraints for dislocation motion [11]. Therefore, bulk values for strengths can be considered as a conservative lower-bound estimate for the strength of microscale structures.

2.3 Identification of material indices

The insulating sidewall of the Rankine micro-engine has two main objectives, which are: (1) to reduce heat loss from the evaporator to the condenser, and (2) to operate without structural damage or failure. These objectives directly affect the performance and reliability of the device. The constraints for this static sidewall are high temperature gradients (hundreds of degrees centigrade over hundreds of microns) and high chamber pressure (approaching one megapascal).

The material indices for this component can be derived by considering the heat loss through the static sidewall, as shown in Figure 2-1. From the one-dimensional Fourier's law of heat conduction, we obtain

$$q = -\left(\frac{dT}{dx}\right)(A)(k). \quad (2.2)$$

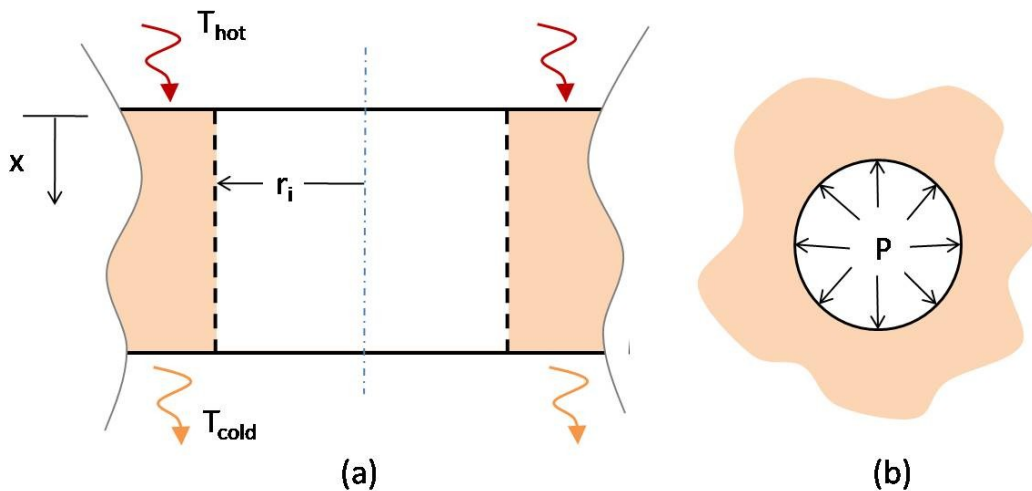


Figure 2-1: (a) Vertical section of the static sidewall showing heat leakage through the structure with r_i as the inner radius. Arrows indicate heat leakages. (b) Horizontal section of the static wall showing P as the internal pressure in the chamber.

Here, q is the flux of thermal energy per unit area per unit time lost through the sidewall, (dT/dx) is the temperature gradient over the vertical length of the wall, A is the horizontal cross-sectional area and k is the thermal conductivity of the material being used. The thermal conductivity k , which represents the material index (hence $\mathbf{M}_1 = \mathbf{k}$) for this particular objective function, must be minimized in order to maximize performance.

The second objective of the static sidewall is to maintain structural integrity while ensuring reduced heat loss. Here we assume that the static sidewall has a cylindrical shape and behaves like a pressure vessel in constraining the chamber pressure. The hoop stress equation can then be used as the constraint equation. For a reliable component, the hoop stress must be less than the strength of the material; that is,

$$\sigma < \left(\frac{Pr_o}{t}\right). \quad (2.3)$$

Here the strength σ is considered because the static sidewall can be assumed to bend and bulge outward due to the internal pressure P ; r_o is the outer radius and t is the thickness of the cylindrical sidewall. The horizontal cross-sectional area A is thus annular. Assuming that the thickness is small compared to the outer radius and eliminating the thickness t using equation (2.3), equation (2.2) can be expressed as

$$q = 2\pi \left(P \frac{dT}{dx}\right) (r_o^2) \left(\frac{k}{\sigma}\right). \quad (2.4)$$

Equation (2.4) shows that the second material index, $M_2 = (k/\sigma)$, must be minimized to maximize performance and reliability.

2.4 Material properties and selection chart

After deriving the material indices, the next step is to collect information on the relevant material properties. Properties of materials at elevated temperatures are required since the goal of the second generation Rankine micro-engine is to run a hot cycle.

An extensive survey of engineering materials revealed that oxides exhibit the lowest thermal conductivities over the temperature range of interest. From Tables 2-1 and 2-2, we can observe that the thermal conductivity of yttria-stabilized zirconia, and silica is ~ 1 W/m/K. Also listed for comparison are the values for metallic alloys (Ti-alloys and Ni-alloys). These materials are commonly used for the components of macroscale heat engines, and exhibit thermal conductivities of ~ 10 W/m/K. Finally, the values for silicon and silicon carbide, which are used in the current generation of microscale heat engines, are also listed.

While thermal conductivity values are readily available, values for the strength of materials of interest at elevated temperatures are not, especially for micromachined specimens. Therefore a preliminary assessment for material selection is made using the strength data reported for bulk specimens (Table 2-3 and Table 2-4).

Table 2-1: Thermal conductivity (W/m/K) of selected oxides, ceramics and alloys at elevated temperatures 298 K – 673 K.

Temperature [K]	298	373	473	673
Zirconia (ZrO ₂) stabilized	1.8*	1.8*	2.0	2.1
Silica (SiO ₂)	1.6*	1.7*	1.63 [†]	1.86
Pyrex, borosilicate [14]	1.16	1.23	1.33	-
Alumina (Al ₂ O ₃)	38*	35*	22.5	13.1
Titania (TiO ₂)	-	9.2*	5.0	3.9
Titanium alloy VT6 [15]	-	6.6	7.8	10.4
Nickel-cobalt alloy [‡]	9.7	10.8	12.4	15.5
Silicon Carbide (SiC)	110*	90*	-	-
Silicon (Si) [13,16]	138	99	78.5	53.6

Table 2-2: Thermal conductivity (W/m/K) of selected oxides, ceramics and alloys at elevated temperatures 773 K – 1273 K.

Temperature [K]	773	873	1073	1273
Zirconia (ZrO ₂) stabilized	2.0*	2.1	2.2	2.2*
Silica (SiO ₂)	2.1*	2.3	-	5.0*
Pyrex, borosilicate [14]	-	-	-	-
Alumina (Al ₂ O ₃)	11*	9.1	7.2	7.0*
Titania (TiO ₂)	4.5*	3.6	3.4	3.3*
Titanium alloy VT6 [15]	11.6	12.9	15.4	17.9
Nickel-cobalt alloy [‡]	17.1	18.6	21.7	24.9
Silicon Carbide (SiC)	65*	-	-	45*
Silicon (Si) [13,16]	46.3	40	30.6	25.6

Data obtained from reference [13] unless mentioned otherwise.

*Reference [12]

[†]Data interpolated from reference [13]

[‡]Nickel-cobalt alloy - Inconel 625 - data obtained from United Performance Metals, 3475 Symmes Road, Hamilton, OH 45015

Table 2-3: Ranges for flexural strength (MPa) of selected oxides and ceramics at elevated temperatures.

Temperature [K]	293	573	773
Zirconia [17]	550 – 770	430 – 480	230 – 330
Silica [18]	90 - 100	-	-
Alumina [19]	330 – 360	320 – 350	300 – 330
Titania [20]	105 – 234	-	-
Quartz [21]	106-190	-	-
Silicon Carbide [22]	510 – 1640	-	-
Silicon [23]	100 – 4000	100 – 2000	100 – 1500

Table 2-4: Yield Strength in units of MPa for selected alloys.

Temperature [K]	Titanium alloy VT6 [15]	Nickel Inconel 625
298	~ 940	~ 496
473	~ 715	~ 464
673	~ 610	~ 429
873	-	~ 410
1073	-	~ 408

Figure 2-2 shows a material selection chart for the materials listed in the tables. The chart represents material property values over the wide range of temperature considered in Tables 2.1, 2.2 and 2.3.

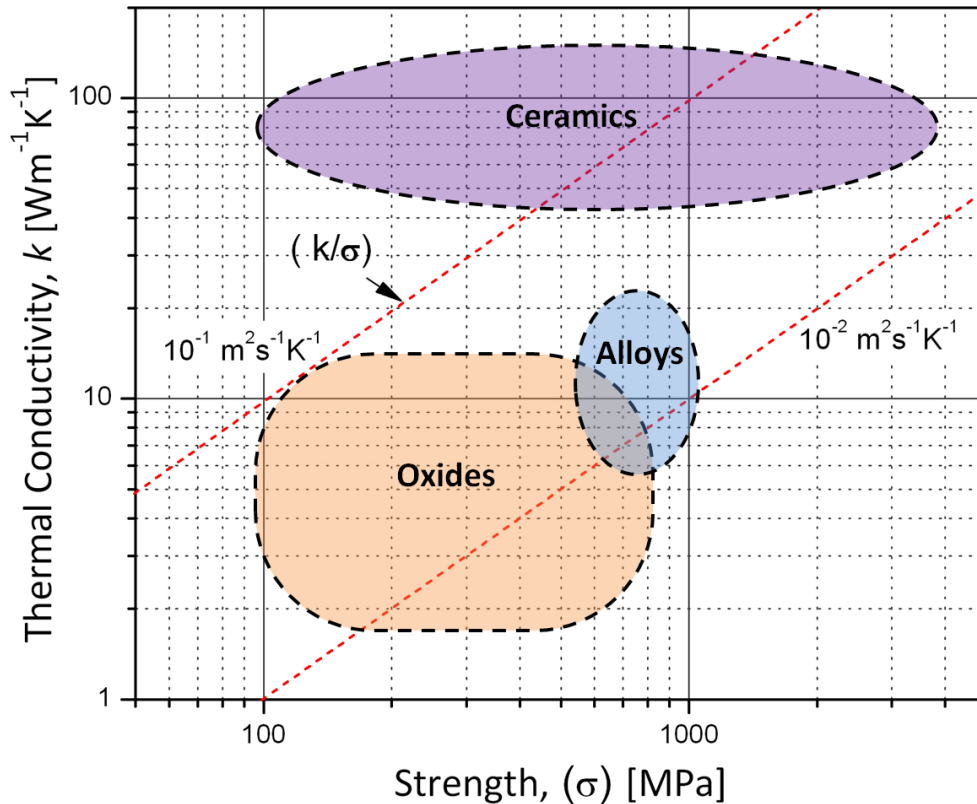


Figure 2-2: Material selection chart based on material properties obtained from published literature over a wide range of temperature. The oxides include zirconia (stabilized), silica, quartz and titania; the alloys are titanium alloy VT6 and nickel-cobalt alloy; and the ceramics are silicon and silicon carbide. The vertical axis represent the first material index, and the red dashed lines represent the second material index.

The vertical axis represents M_1 , and the red dotted line represents M_2 .

Figure 2-2 indicates a trade-off between performance and reliability: oxides have the lowest thermal conductivity, but alloys and ceramics exhibit higher strength.

2.5 Summary

In this chapter, the use of the Ashby methodology was demonstrated by applying it for the preliminary selection of materials for the static sidewalls. The primary metric for improving performance is to select materials with low thermal conductivities. A survey of engineering materials indicates that oxides (zirconia and silica) are the best candidates. However, the sidewalls must also withstand the stresses created by thermomechanical and pressure loads during operation, and oxides are prone to brittle fracture. Therefore, in qualitative terms, these materials offer high performance but low reliability. In contrast, titanium alloys and nickel-based alloys exhibit higher values for both conductivity and strength. Therefore, these materials offer a compromise between moderate performance and sufficient strength. In addition to performance and reliability, the third consideration is that of manufacturability. Few techniques are available at present to deep etch oxides and alloys, and to bond them to create the shapes shown in Figure 1-2. However, the ceramics, especially single-crystal silicon, can be micromachined with relative ease. Therefore, these materials offer excellent manufacturability, but poor performance and low reliability.

All the conclusions drawn in this chapter are qualitative in nature. The next step is to quantify the trade-off between performance, reliability, and manufacturability by undertaking detailed thermal and mechanical analysis for the materials of interest: zirconia, silica, titanium alloy, nickel-cobalt alloy, silicon carbide and silicon.

Chapter 3 – Analytical Models for Heat Transfer and Deformation

This chapter details simplified analytical models for the thermal and mechanical behaviour of the static sidewall to analyze the performance and reliability of the Rankine micro-engine. The thermal analysis assumes one-dimensional Fourier heat transfer to model the heat loss through the static sidewall; this model can be used to evaluate the effects of different materials and shape on performance. Subsequently, three analytical models of increasing complexity are developed in order to identify materials and geometry that will withstand the stresses generated within the static sidewall.

3.1 Thermal analysis of the static sidewall

The static sidewall is the only structure that is in contact with both the hot and cold surfaces of the Rankine micro-engine. Hence, this structure acts as the dominant thermal path for heat leakages to occur from the evaporator to the condenser. To model this, we can use Fourier's law of heat conduction in one dimension, and the rate of heat loss can be expressed as

$$\dot{Q}_{loss} = (\Delta T) \left(\frac{kA}{L} \right). \quad (3.1)$$

Here, k is the thermal conductivity of the static sidewall, L is the distance between the hot and cold surfaces, and A is the contact area of the static sidewall with the hot/cold surfaces. Assuming that the only heat loss for the thermodynamic cycle occurs through the static sidewall, and that the rest of the heat extracted from the evaporator is converted to useful power, the efficiency, η , is given by¹

$$\eta = \left(\frac{w_{electric}}{\dot{Q}_{evaporator} + \dot{Q}_{loss}} \right). \quad (3.2)$$

Here $w_{electric}$ is the electric output power, and $\dot{Q}_{evaporator}$ is the heat provided by the evaporator. Substituting equation 3.1 into equation 3.2, we can link the efficiency of the device with the material properties and geometry of the static sidewall.

In the first generation Rankine micro-engine, the static sidewall was made of high- k material (single-crystal silicon) and spanned the entire chip surface, which has an area of $\sim 1 \text{ cm}^2$ (Figure 1.2 & Figure 3.1(a)). While this setup was appropriate for assessing turbomachinery at room temperature, it is not suitable for high temperature operation because this design of the sidewall provides the maximum contact area for heat leakage. Therefore, the first step in reducing heat loss is to reduce the contact area of the static sidewall by changing the geometry. One option is an annular cylinder with a thickness, t , of $200 \text{ }\mu\text{m}$, as shown in Figure 3-1(b). (The effective areas of the pillars are negligible in comparison to the area of the cylinder).

¹ M. Liamini, Université de Sherbrooke (Personal communication).

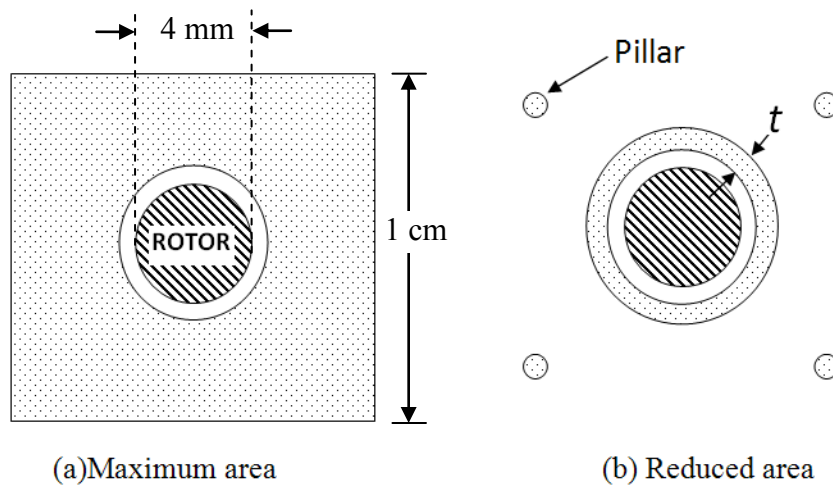


Figure 3-1: Cross-sectional area of the static sidewall surrounding the rotor. (a) Top view of the maximum possible area of the wall for the entire chip. (b) Top view of a cylindrical wall of thickness t .

The second step in reducing the heat loss is to use materials with low thermal conductivity already identified through the Ashby approach. Figure 3-2 shows the effect of contact area and thermal conductivity on efficiency.

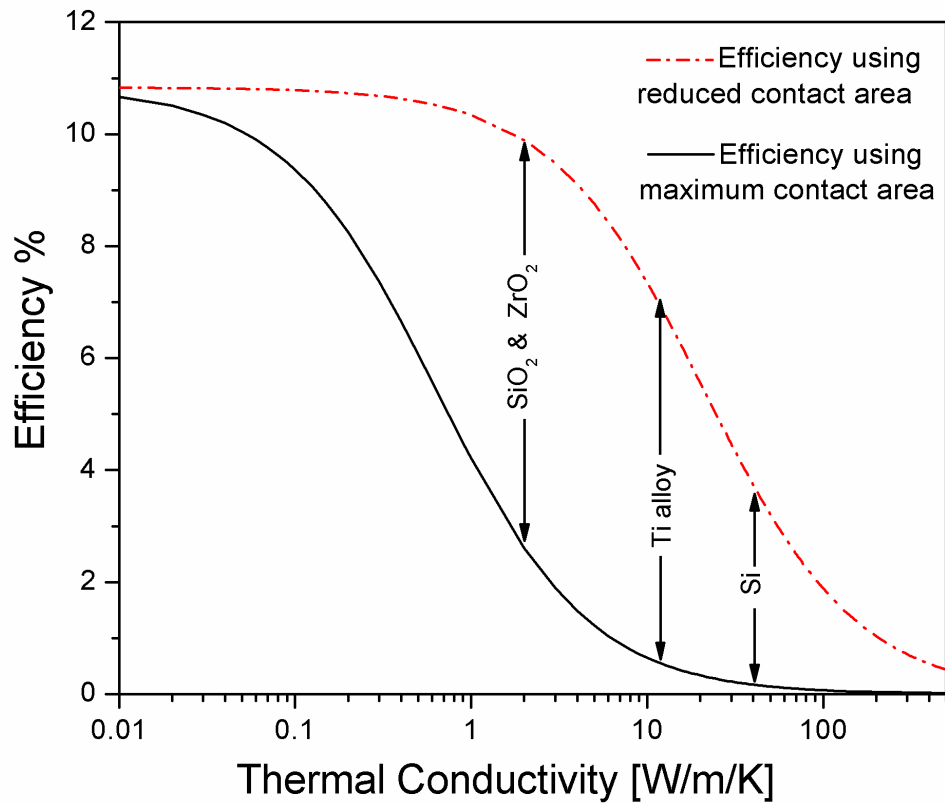


Figure 3-2: Thermal efficiencies of the Rankine micro-engine for a power output of ~8 W. The curves represent the variation of thermal efficiencies as a function of thermal conductivity for two area configurations. Arrows show the range of efficiencies that can be obtained using different materials. The values indicated correspond to thermal conductivities at 773 K.

The region between the two curves in Figure 3-2 represents a design space in terms of material property and geometry for the static sidewall. Materials with low thermal conductivities (silica and zirconia) enable a larger design space with significantly higher efficiencies as opposed to materials with high thermal conductivities (such as single-crystal silicon). Titanium alloys occupy a design space in between the ceramics and the oxides. Thus, Figure 3-2 acts as a guide in choosing materials and geometry (of the assumed cylindrical shape) for the static

sidewall. It can be concluded that zirconia and silica enable efficiencies of up to 10% (almost three times that of silicon) and an annular cylindrical wall provides a simple way of reducing contact area. Similar calculations can be performed to explore the effects of other wall geometries.

Using equation (3.2), we can calculate the maximum thickness of the annular cylinder for the selected materials for a device efficiency of 10%. The values shown in the plot in Figure 3-3 were obtained using thermal conductivity values at 773 K.

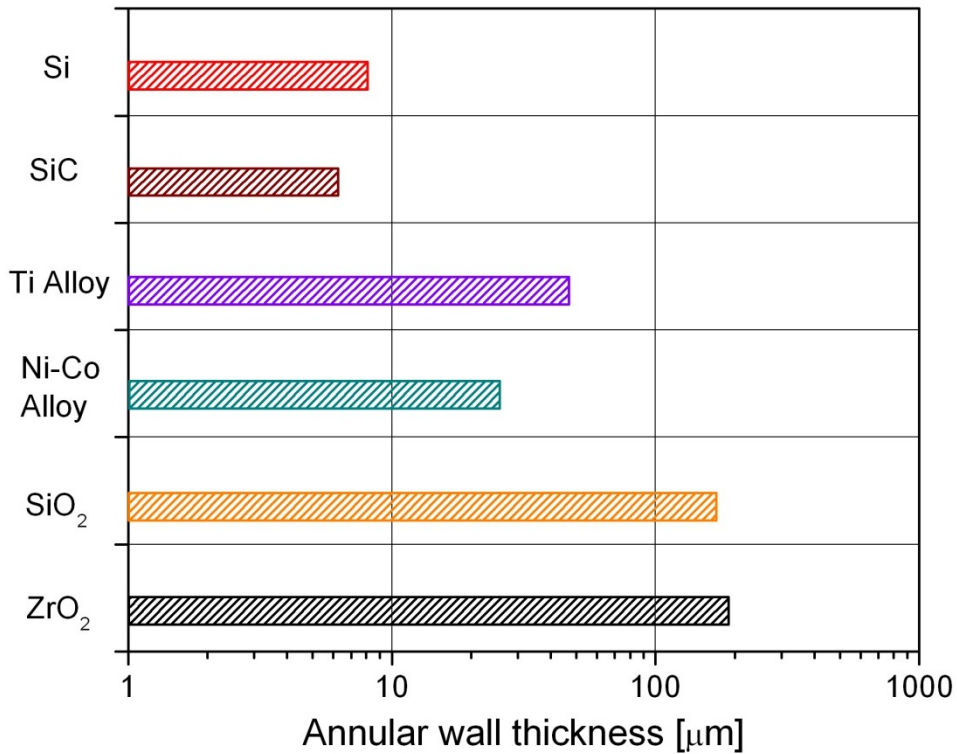


Figure 3-3: Range of annular wall thicknesses for different materials generating device efficiency of at least 10%. Silica and zirconia has a larger thickness range compared to silicon and silicon carbide.

From Figure 3-3, we can conclude that annular walls with a thickness of about 150 μm can be constructed using silica and zirconia, while still achieving a high device efficiency of 10%. In contrast, the corresponding wall thickness for Si and SiC is less than 10 μm .

3.2 Stress analysis for static sidewall

Having established a shape for the static sidewall, it is necessary to quantify the stresses experienced by this structure during engine operation. The static sidewall is analyzed using three analytical models of increasing complexity: Euler-Bernoulli beam analysis; two-dimensional (2D) plane strain elasticity; and three-dimensional (3D) shell theory. The reasons for undertaking these three models are that the beam analysis enables us to identify stresses in the axial direction, the plane strain elasticity helps us understand the stresses in the radial direction, and the shell theory gives us an idea of the stress field at various positions of the static sidewall. For the plane strain analysis and the shell theory analysis, we will also consider the thermal effects on the stresses in the static sidewall. These different models therefore represent a trade-off between simplicity and accuracy.

Figure 3-4 shows a schematic illustration of the cylindrical sidewall, along with a view of the vertical section (Figure 3-4(a)), a horizontal section (Figure 3-4(b)), and a 3D view (Figure 3-4(c)) of the static sidewall.

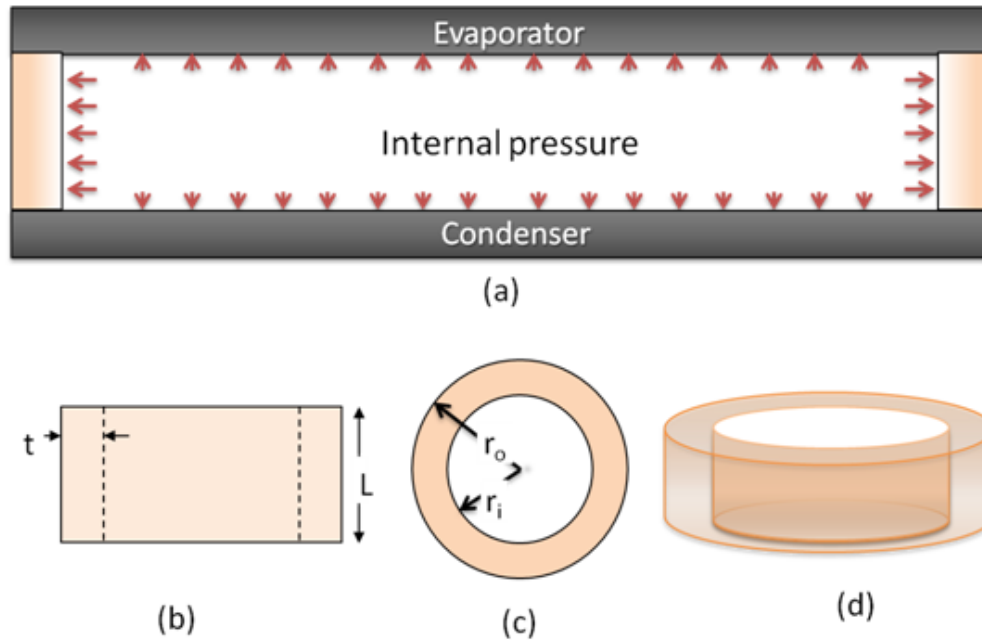


Figure 3-4: The static sidewall (not to scale). (a) Vertical section of the static sidewall bonded to the evaporator and condenser. (b) Vertical section showing sidewall thickness t and its length L . (c) Horizontal section showing the inner radius r_i and outer radius r_o . (d) A 3D view of the static wall.

3.2.1 Euler-Bernoulli beam analysis

The first analytical model implemented for the sidewall is the Euler-Bernoulli beam model. Here we consider a differential element of the annular wall in the vertical section (Figure 3-5). This differential element is then considered as a uniform Euler-Bernoulli beam.

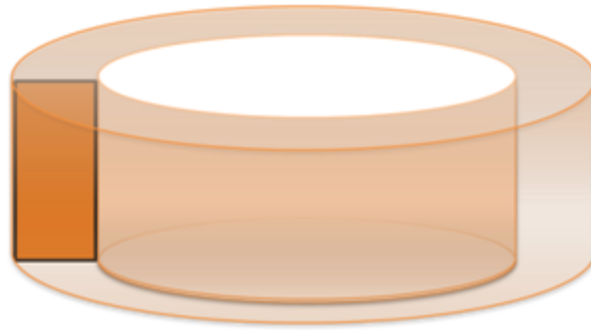


Figure 3-5: Differential element (rectangular orange) of the sidewall assumed to be a beam.

The sidewall is bonded to the hot evaporator and the cold condenser; hence, the beam is modelled with both ends clamped. The loads and deformations experienced by the sidewall are due to the fluidic pressure, which is assumed to be uniform.

This beam model can be easily analyzed using simple formulas for stress and deformation [24]. However, it must be emphasized that this is only a first step because the model over-simplifies the geometry and neglects any transverse shear strains that might be significant as the length to thickness ratio is less than 10 [24, 25]. First, let us consider the stresses generated due to the applied pressure.

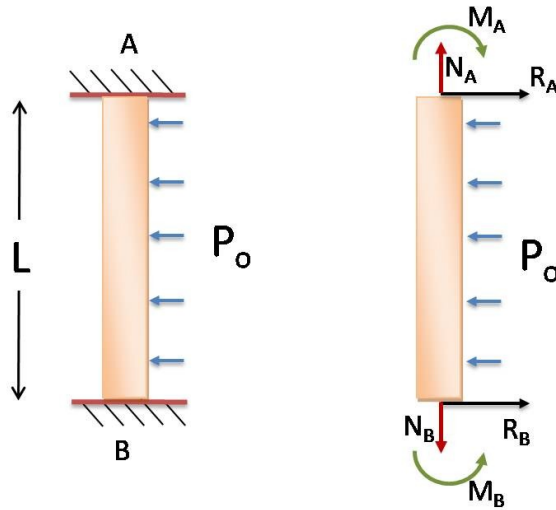


Figure 3-6: (a) Axial differential element of the sidewall assumed as a clamped-clamped beam with a distributed load of P_o . (b) Free-body diagram of the clamped-clamped beam.

The moment generated at the clamped edges (Figure 3-6) due to the distributed load P_o is given by

$$M_A = M_B = \frac{P_o L^2}{12}, \quad (3.3)$$

where M_A is the magnitude of the moment applied to the beam. This moment gives rise to the maximum stress on the beam at the clamped edge, given by

$$\sigma_x = \frac{M_A t}{2I}, \quad (3.4)$$

where t is the thickness of the beam. Substituting the expression for the area moment of inertia for a beam with a rectangular cross-section, we obtain

$$\sigma_x = \left(\frac{P_o}{2}\right) \left(\frac{L}{t}\right)^2. \quad (3.5)$$

Therefore, for a given length L , the stress along the beam is inversely proportional to the square of the thickness, which implies that a thinner sidewall will experience a greater stress.

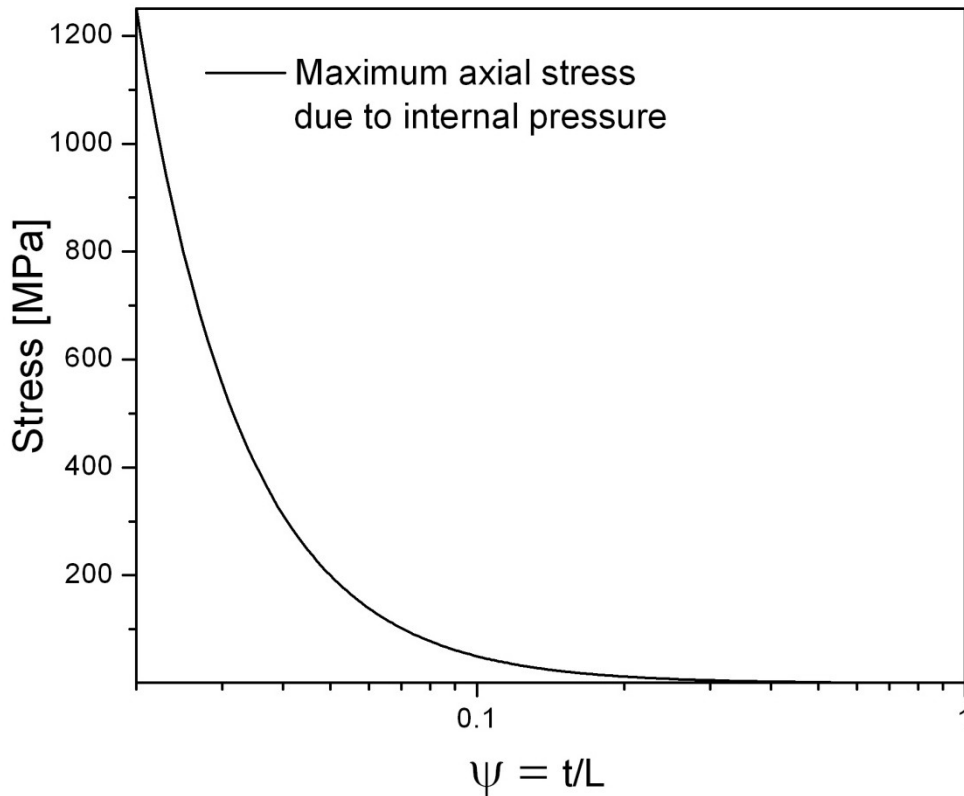


Figure 3-7: Variation of stress as a function of the thickness-to-length ratio, ψ , for zirconia. For a fixed wall length, the stress due to internal pressure dominates for thinner sidewall, and the stress due to deflected end dominates for thicker walls.

For sidewalls less than 50 μm thick, the stress due to internal pressure is considerable. Hence the curve in Figure 3-8 can be used as a guide to determine the minimum thickness of the sidewall necessary to ensure reliability of the device for different materials. These values of minimum wall thickness can be merged with the thickness range for efficiency (Figure 3.3) to create Figure 3-8.

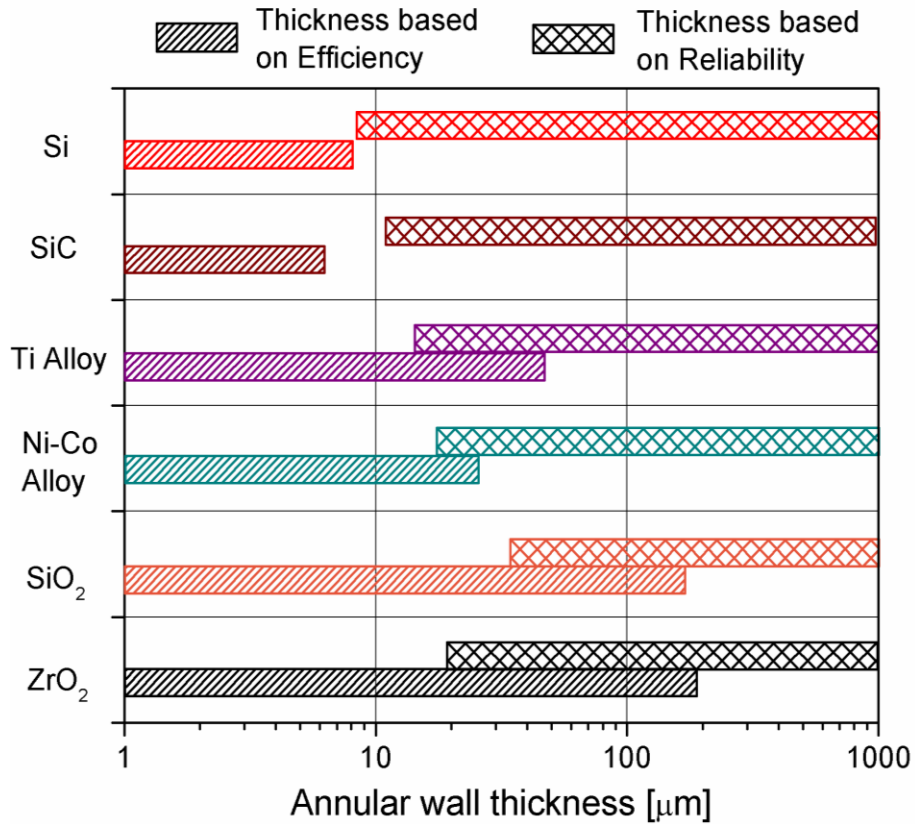


Figure 3-8: Design space for static sidewall thickness for selected ceramics, alloys and oxides. The bars on the left indicate thickness range satisfying 10% efficiency, and those on the right indicate thickness ensuring reliability for an internal pressure of 1 MPa.

In Figure 3-8, we notice that for a 10% efficient device, silicon and silicon carbide exhibit a null design space. The alloys and oxides, on the other hand, have overlapping regions for thicknesses, indicating viable design spaces; of these, silica and zirconia possess the largest design space. Figure 3-8 can therefore be used for selecting materials and geometry for more advanced modeling and analysis.

3.2.2 Plane strain elasticity

The linear theory of elasticity is a mathematical model for the deformation of solids in the limit of small deformations. This model leads to governing equations in the form of partial differential equations, and the solutions of these equations lead to the determination of stresses and strains within the structure. Here, a 2D plane strain elasticity model is applied to the horizontal section of this sidewall (Figure 3.4c), assuming that: (1) deformations are small; (2) analysis is restricted to linear elastic solids; and (3) the displacements are single valued. Further, the static sidewall is modeled as an axisymmetric annular cylinder. To simplify the analysis, the end effects of the cylinder, which may be significant, are neglected.

The goal of this analysis is to evaluate the mechanical and thermomechanical stresses separately, and then compare between the two. Thus, the analysis is divided into two parts. The first part deals with the stresses generated due to internal pressure while the second part deals with the stresses generated due to a temperature difference.

3.2.2.1 Stress due to internal pressure

The following steps were implemented in order to derive the equations that dictate the stresses for the horizontal section [26]. First the displacement tensor and strain compatibility equations in cylindrical co-ordinates were defined, followed by the governing partial differential equations for force equilibrium.

These field equations were then coupled using the constitutive relations for linear elastic deformation (Hooke's Law). Using plane strain, continuous displacement, and axisymmetric assumptions to simplify the stress formulation (Beltrami-Michell compatibility relations), and employing Airy's stress function $\phi(r,\theta)$ as a solution to the 2D stress field, the stresses in the structure can be obtained as:

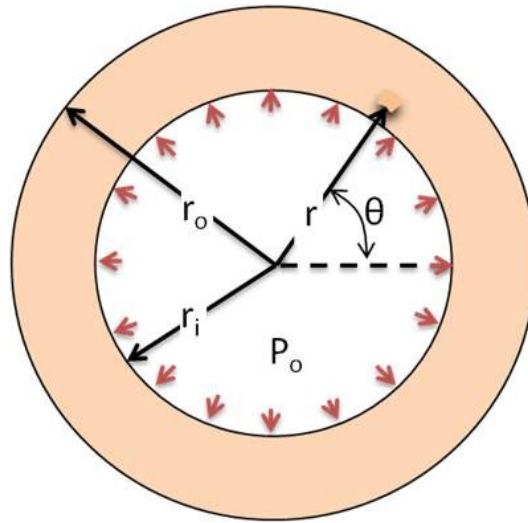


Figure 3-9: Schematic of the static sidewall for the 2D plane strain analysis. P_o is the internal pressure. r_i and r_o are the inner and outer radii respectively. The ambient pressure (atmospheric) is considered much smaller than the internal chamber pressure and is thus neglected.

$$\sigma_r = \frac{A}{r^2} + B \quad (3.6a)$$

$$\sigma_\theta = -\frac{A}{r^2} + B \quad (3.6b)$$

$$\tau_{r\theta} = 0 \quad (3.6c)$$

$$\sigma_z = \nu(\sigma_r + \sigma_\theta) \quad (3.6d)$$

The constants, A and B were determined by applying the boundary conditions shown in Figure 3-9. The maximum stress occurs on the internal surface of the annular structure. Hence, setting $r = r_i$, the maximum dimensionless stresses are:

$$\frac{\sigma_r}{P_o} = -\left(\frac{\xi^2 + 1}{\xi^2 - 1}\right) \quad (3.7a)$$

$$\frac{\sigma_\theta}{P_o} = \left(\frac{\xi^2 + 1}{\xi^2 - 1}\right) \quad (3.7b)$$

$$\frac{\sigma_z}{P_o} = \left(\frac{2\nu}{\xi^2 - 1}\right) \quad (3.7c)$$

Here, $\xi = r_o/r_i$.

3.2.2.2 Stress due to temperature difference

For the proposed Rankine micro-engine to run a hot cycle, the inner surface of the static sidewall will be subjected to high temperatures due to the presence of superheated vapour within the chamber. Since the outer surface of the wall is assumed to be in contact with ambient air, it is necessary to identify the magnitude of the stresses generated within the sidewall due to the temperature difference. Using Airy's stress function, and assuming a steady state temperature field, the radial distribution of the temperature $T(r)$ can be expressed as [26]

$$T(r) = \frac{\Delta T}{\log\left(\frac{r_o}{r_i}\right)} \log\left(\frac{r_o}{r}\right), \quad (3.8)$$

where ΔT is the temperature difference between the inner and outer surface of the sidewall. The thermal stresses generated by this temperature field are given by [27]

$$\sigma_r = \left(\frac{\alpha E}{1-\nu}\right) \left(\frac{1}{r^2}\right) \left[\left(\frac{r^2 - r_i^2}{r_o^2 - r_i^2} \int_{r_i}^{r_o} T r dr\right) - \int_{r_i}^r T r dr \right] \quad (3.9a)$$

$$\sigma_\theta = \left(\frac{\alpha E}{1-\nu}\right) \left(\frac{1}{r^2}\right) \left[\left(\frac{r^2 + r_i^2}{r_o^2 - r_i^2} \int_{r_i}^{r_o} T r dr\right) - \int_{r_i}^r T r dr - T r^2 \right] \quad (3.9b)$$

$$\sigma_z = \left(\frac{\alpha E}{1-\nu}\right) \left[\left(\frac{2}{r_o^2 - r_i^2} \int_{r_i}^{r_o} T r dr\right) - T \right]. \quad (3.9c)$$

Here, α is the co-efficient of thermal expansion, E is the Young's modulus, and ν is the Poisson's ratio. The variation of the dimensionless thermal stress variation as a function of radius (for a given internal radius) is shown in the plot in Figure 3-10.

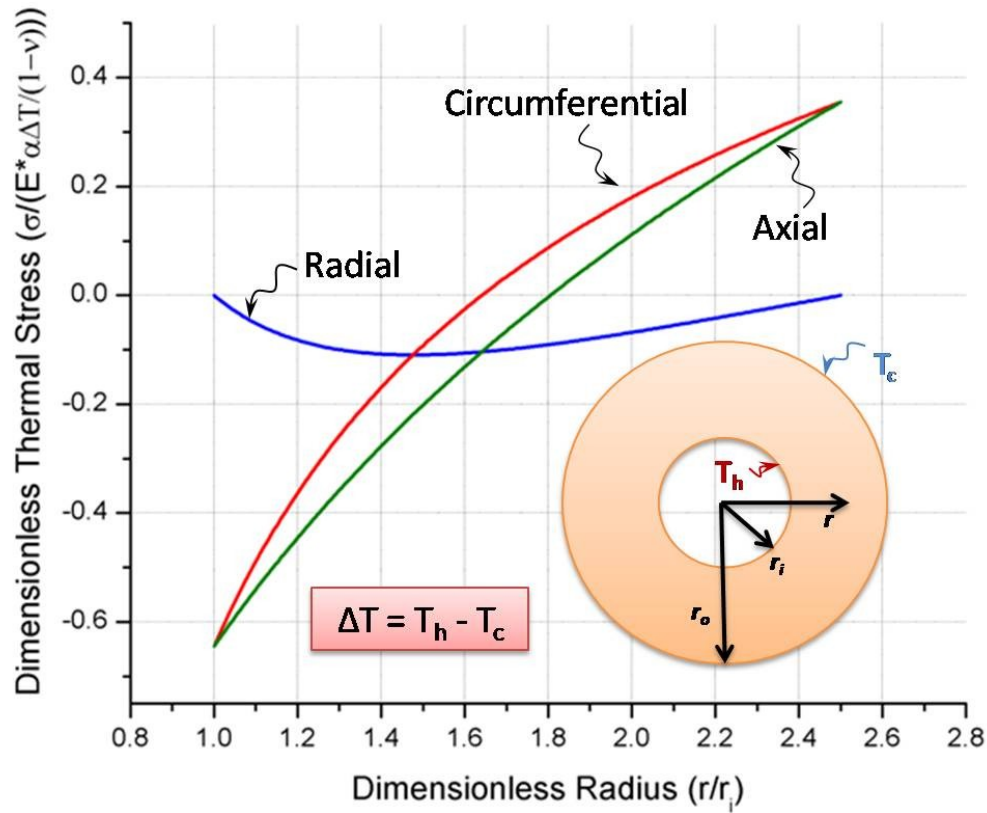


Figure 3-10: Dimensionless thermal stress variation for the three stress components in the radial direction as a function of dimensionless radii. Maximum stresses occur on the inner surface.

We can now plot the dimensionless mechanical and thermal stresses, as shown in Figure 3-11, in order to compare the effect of geometry on the magnitude of these stresses.

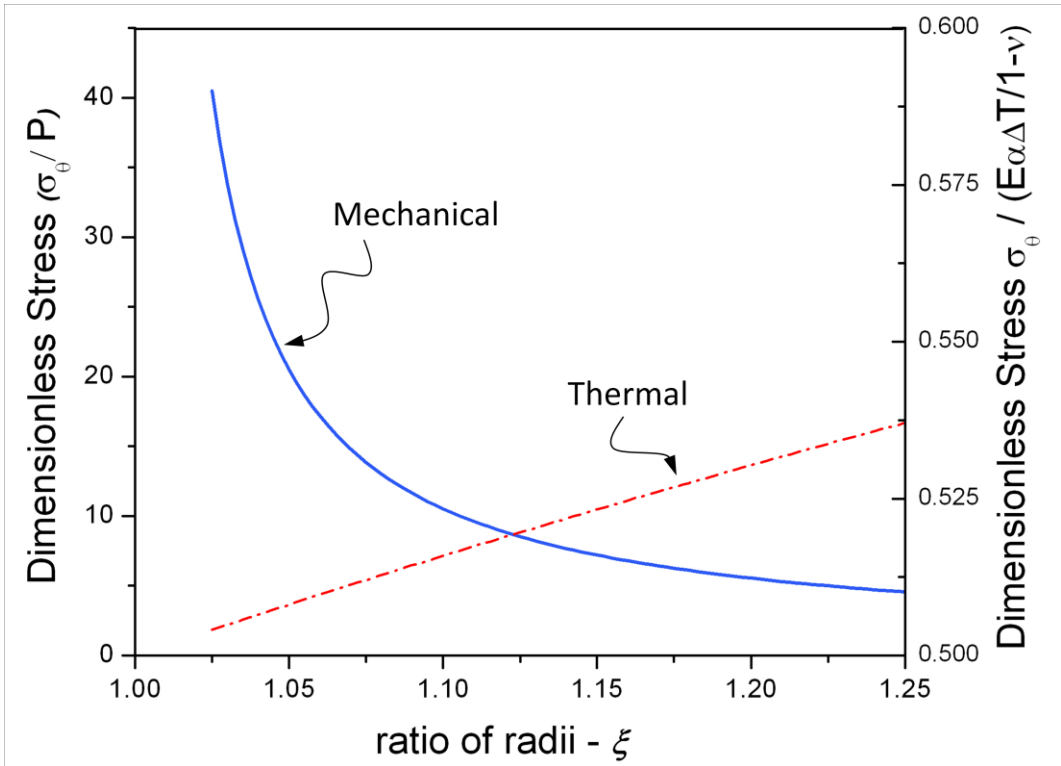


Figure 3-11: Dimensionless circumferential stresses as a function of the ratio of radii for the static sidewall. The dimensionless mechanical stress is higher than the dimensionless thermal stress for smaller ratios (thinner sidewall).

The normalizing factors for mechanical and thermal stresses are comparable in magnitude assuming operating conditions that lead to an internal pressure P of ~ 1 MPa, and a temperature difference, $\Delta T \sim 1$ K. (The value of ΔT is small because the fluid surrounding the sidewall is assumed to be air, which is an extremely good insulator. Hence, there is essentially no heat transfer in the radial direction and the temperatures on the inner and outer surface of the sidewall are very nearly the same.) Under these conditions, $\left(\frac{E\alpha\Delta T}{1-\nu}\right) \sim 1$ MPa. Therefore, we can conclude from Figure 3-12 that the stress due to internal pressure is the

dominant stress. However, this analysis is still too simple to capture the stress field of a three dimensional structure, and is limited by the assumption of treating the static sidewall as a long cylinder.

3.2.3 Shell Theory

The shell theory is an extension of the beam theory and is used to analyze the deformations of an object with two dimensions being far greater than the third. The governing partial differential equations are developed from continuum mechanics and simplified by neglecting vertical/transverse shear strains (Kirchhoff's hypothesis for plates). This enables stress resultants and stress couples of the neutral surface of the structure to be evaluated. The stress at a point in the structure can then be approximated using these stress resultants and stress couples.

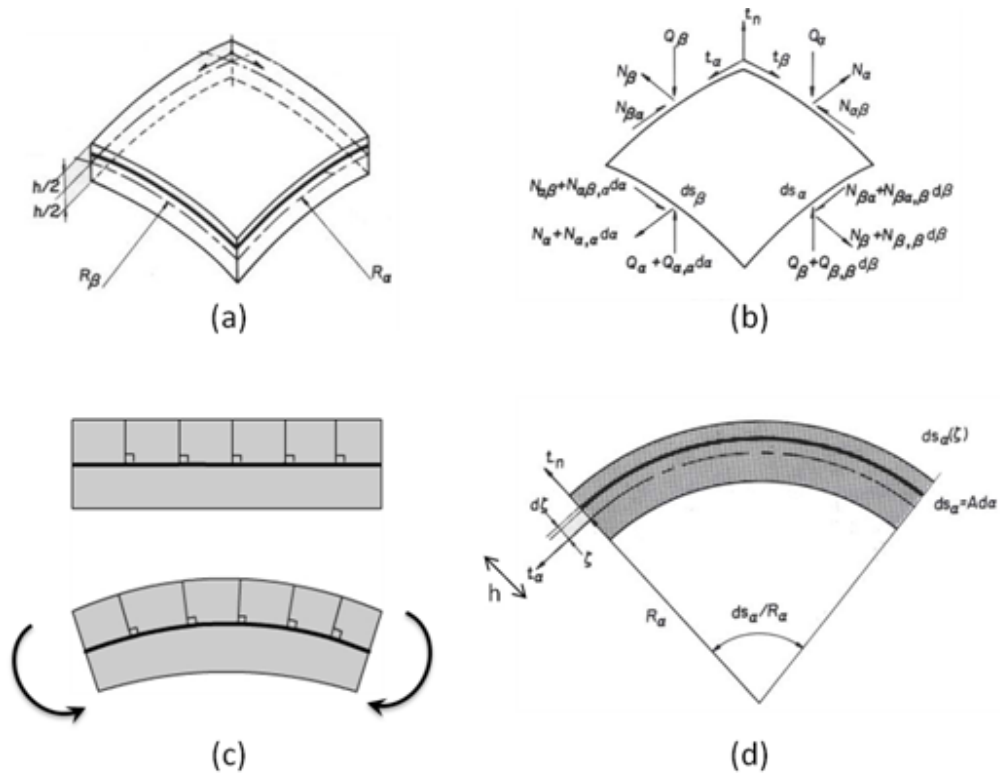


Figure 3-12: (a) A shell element with radii of curvature R_α and R_β much larger than the thickness h . (b) The stress resultants per unit length obtained by integrating out the thickness. (c) Kirchoff's hypothesis of straight normals, a critical assumption in the shell theory. (d) A section of the curved surface indicating the estimation of the stresses of a plane ζ distance from the middle surface.

Figure 3-12 shows the various aspects of the shell theory. In addition to the assumptions used to develop the shell theory equations, the following assumptions are also made while obtaining the governing equation for the static sidewall. Materials are restricted to linear elastic solids and the structure is considered axisymmetric. The shell is assumed as a short cylinder with its length less than the "half-wave length of bending," which is the length at which a given shell is considered as long and, therefore, treatable by the semi-infinite approach,

and that the edges are clamped at the top and bottom. The thermal field and body forces are neglected.

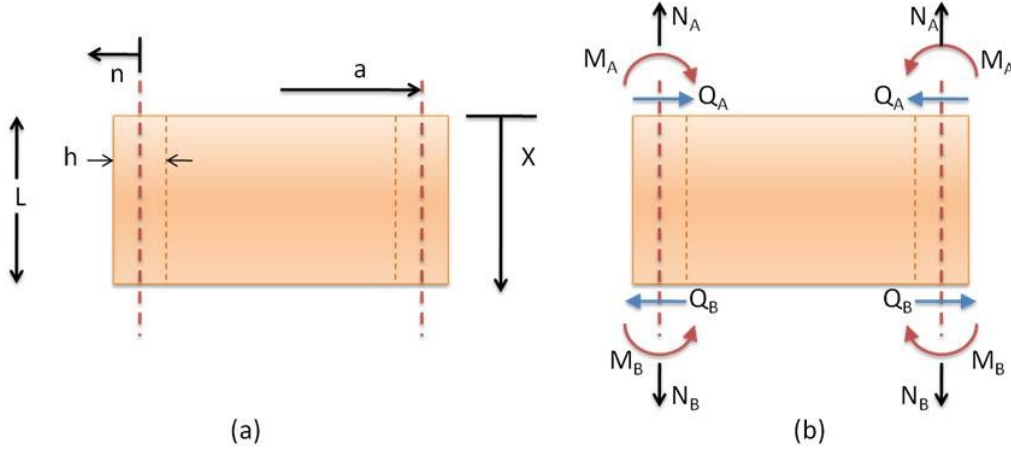


Figure 3-13: (a) Vertical section of the sidewall with thickness h . (b) The stress and moment resultants of the neutral.

Figure 3-13 shows the vertical section of the static sidewall and the relevant dimensions used in the governing equations of the shell theory, which can be expressed as

$$D \frac{\partial^4 D_n}{\partial x^4} + \frac{Eh}{a^2} D_n = q_n + \frac{\nu}{a} [N_x(0)], \quad (3.10)$$

where

$$D = \frac{Eh^3}{12(1-\nu)} \quad (3.11)$$

Here D_n is the deflection of the middle/neutral surface of the sidewall, D is the flexural rigidity, q_n is equivalent to the internal pressure within the chamber and $N_x(0)$ is the constant axial force on the middle surface equivalent to $(P_o a/2)$, E is

the Young's modulus, h is the thickness of the sidewall and a is the radius of the neutral surface. The deflection of the neutral surface can be expressed as the sum of the homogeneous and particular solution of the governing equation. Thus,

$$D_n = D_{nh} + D_{np} . \quad (3.12)$$

The homogenous solution is given by

$$D_{nh} = [C_1 F_1(kx) + C_2 F_2(kx)] + [C_3 F_3(kx) + C_4 F_4(kx)] , \quad (3.13)$$

where

$$F_1(kx) = e^{-kx}[\cos(kx)]$$

$$F_2(kx) = e^{-kx}[\sin(kx)]$$

$$F_3(kx) = e^{kx}[\cos(kx)]$$

$$F_4(kx) = e^{kx}[\sin(kx)] \quad (3.14)$$

and

$$k = \frac{Eh}{4Da^2} . \quad (3.15)$$

The particular solution is given by

$$D_{np} = \frac{P_1 a^2}{Eh} \left(1 - \frac{\nu}{2}\right) . \quad (3.16)$$

Substituting D_n into equation (3.10) and using the boundary conditions $D_n(x=0) = D_n(x=L) = 0$, we arrive at a system of equations which can be expressed as

$$[C] = -\frac{1}{2k^2D}[F]^{-1}[B]. \quad (3.17)$$

The matrices $[C]$, $[F]$ and $[B]$ are defined as

$$[C] = \begin{bmatrix} C_1 \\ C_2 \\ C_3 \\ C_4 \end{bmatrix}, [B] = \begin{bmatrix} M_A \\ Q_A \\ M_B \\ Q_B \end{bmatrix},$$

and

$$[F] =$$

$$\begin{bmatrix} 0 & -1 & 0 & 1 \\ k & k & -k & k \\ F_2(kL) & -F_1(kL) & -F_4(kL) & F_3(kL) \\ k(F_1(kL) - F_2(kL)) & k(F_1(kL) - F_2(kL)) & k(F_1(kL) - F_2(kL)) & k(F_1(kL) - F_2(kL)) \end{bmatrix}.$$

Defining $[F]^{-1}$ to be as

$$[F]^{-1} = \begin{bmatrix} f(1,1) & f(1,2) & f(1,3) & f(1,4) \\ f(2,1) & f(2,2) & f(2,3) & f(2,4) \\ f(3,1) & f(3,2) & f(3,3) & f(3,4) \\ f(4,1) & f(4,2) & f(4,3) & f(4,4) \end{bmatrix},$$

and using equation (3.17), the constants can be expressed as

$$C_1 = -\frac{1}{2k^2D} [M_A(f(1,1)) + Q_A(f(1,2)) + M_B(f(1,3)) + Q_B f(1,4)] \quad (3.18a)$$

$$C_2 = -\frac{1}{2k^2D} [M_A(f(2,1)) + Q_A(f(2,2)) + M_B(f(2,3)) + Q_B f(2,4)] \quad (3.18b)$$

$$C_3 = -\frac{1}{2k^2D} [M_A(f(3,1)) + Q_A(f(3,2)) + M_B(f(3,3)) + Q_B f(3,4)] \quad (3.18c)$$

$$C_4 = -\frac{1}{2k^2D} [M_A(f(4,1)) + Q_A(f(4,2)) + M_B(f(4,3)) + Q_B f(4,4)]. \quad (3.18d)$$

The expressions of the constants are then substituted into equation (3.13). We then collect the moment and shear terms and represent them as

$$D_{nh}(x = 0) = [M_A P_1 + Q_A P_2 + M_B P_3 + Q_B P_4] . \quad (3.19)$$

Here the coefficients P_1, P_2, P_3 and P_4 are defined as

$$P_1 = -\frac{1}{2k^2 D} ([F_1(0)f(1,1)] + [F_2(0)f(2,1)] + [F_3(0)f(3,1)] \\ + [F_4(0)f(4,1)]) \quad (3.20a)$$

$$P_2 = -\frac{1}{2k^2 D} ([F_1(0)f(1,2)] + [F_2(0)f(2,2)] + [F_3(0)f(3,2)] \\ + [F_4(0)f(4,2)]) \quad (3.20b)$$

$$P_3 = -\frac{1}{2k^2 D} ([F_1(0)f(1,3)] + [F_2(0)f(2,3)] + [F_3(0)f(3,3)] \\ + [F_4(0)f(4,3)]) \quad (3.20c)$$

$$P_4 = -\frac{1}{2k^2 D} ([F_1(0)f(1,4)] + [F_2(0)f(2,4)] + [F_3(0)f(3,4)] \\ + [F_4(0)f(4,4)]) \quad (3.20d)$$

We perform the same exercise for $D_{nh}(x = L), D'_{nh}(x = 0)$ and $D'_{nh}(x = L)$ and using the boundary conditions of no deflection and rotation at the clamped edges, we arrive at the system of equations given by

$$\begin{bmatrix} P_1 & P_2 & P_3 & P_4 \\ Q_1 & Q_2 & Q_3 & Q_4 \\ R_1 & R_2 & R_3 & R_4 \\ S_1 & S_2 & S_3 & S_4 \end{bmatrix} \begin{bmatrix} M_A \\ Q_A \\ M_B \\ Q_B \end{bmatrix} = \begin{bmatrix} -D_{np}(0) \\ -D_{np}(L) \\ 0 \\ 0 \end{bmatrix}, \quad (3.21)$$

where the elements in [Q], [R] & [S] are obtained in the same manner as [P]. Hence, M_A , Q_A , M_B and Q_B can be evaluated. Since this model assumes a clamped edge, the maximum stresses occur at the edges and are given by

$$\sigma_x = \frac{N_x}{h} \pm \frac{6M_x}{h^2} \quad (3.22a)$$

$$\sigma_\theta = \frac{N_\theta}{h} \pm \frac{6M_\theta}{h^2} \quad (3.22b)$$

$$\sigma_{shear} = \frac{3Q_A}{2h} \quad (3.22c)$$

Here, $M_A = M_x = M_\theta$, $N_x = \frac{P_o a}{2}$, $N_\theta(x) = \nu N_x + \left(\frac{Eh}{a} D_n(x)\right)$.

At this stage, a MATLAB code is used to obtain the stresses at various locations along the length of the annular sidewall. As a check, stresses computed for the representative case of a silica wall of length 0.01 m are compared with the hoop stress and longitudinal stress predicted by plane strain elasticity.

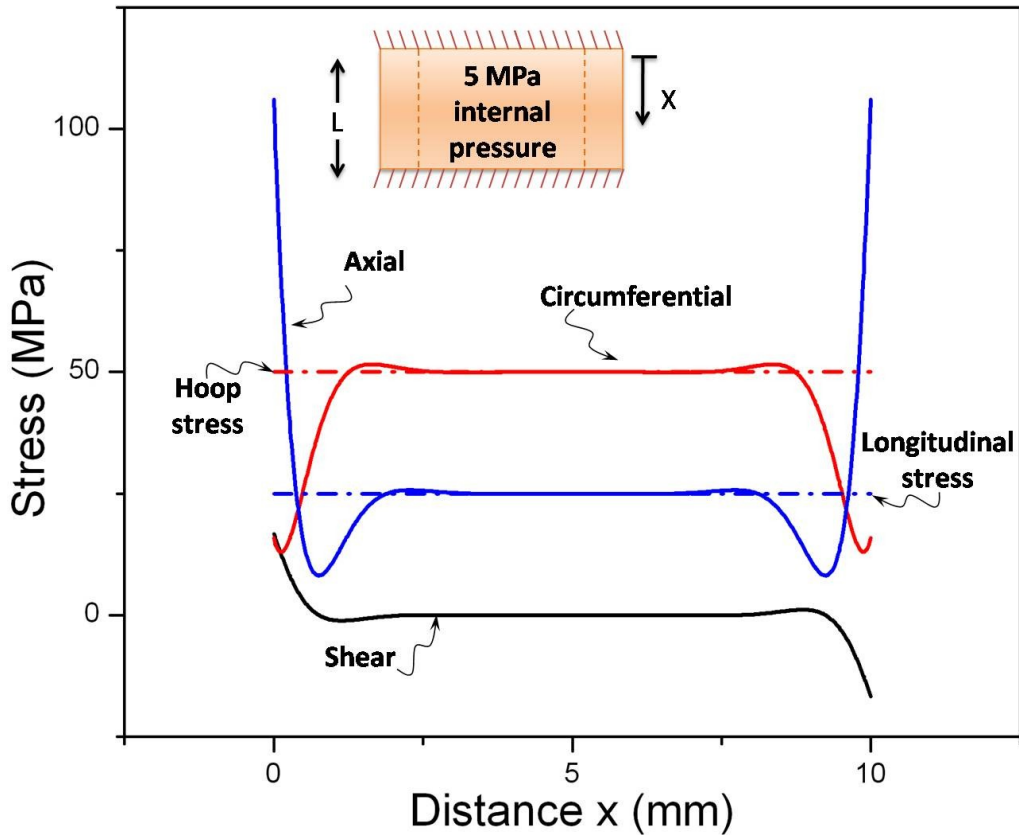


Figure 3-14: Solid lines represent the stresses on the inner surface of the sidewall. Thickness is taken to be $200 \mu\text{m}$ and the internal pressure is 5 MPa . The dash-dot-dash lines represent the hoop and the longitudinal stresses for a long pressure vessel obtained from plane-strain elasticity.

The axial and circumferential stresses are in excellent agreement with the hoop stress and longitudinal stress, respectively, away from the edges. However, the axial stresses at the edges are much higher, compared to the other stresses, as the homogenous part of the deflections equation D_{nh} is more influential near the edges.

Using the MATLAB code, we proceed to evaluate the stresses for the shell model of the static sidewall for various lengths. Figure 3-15 shows four plots for the annular cylinder with different lengths.

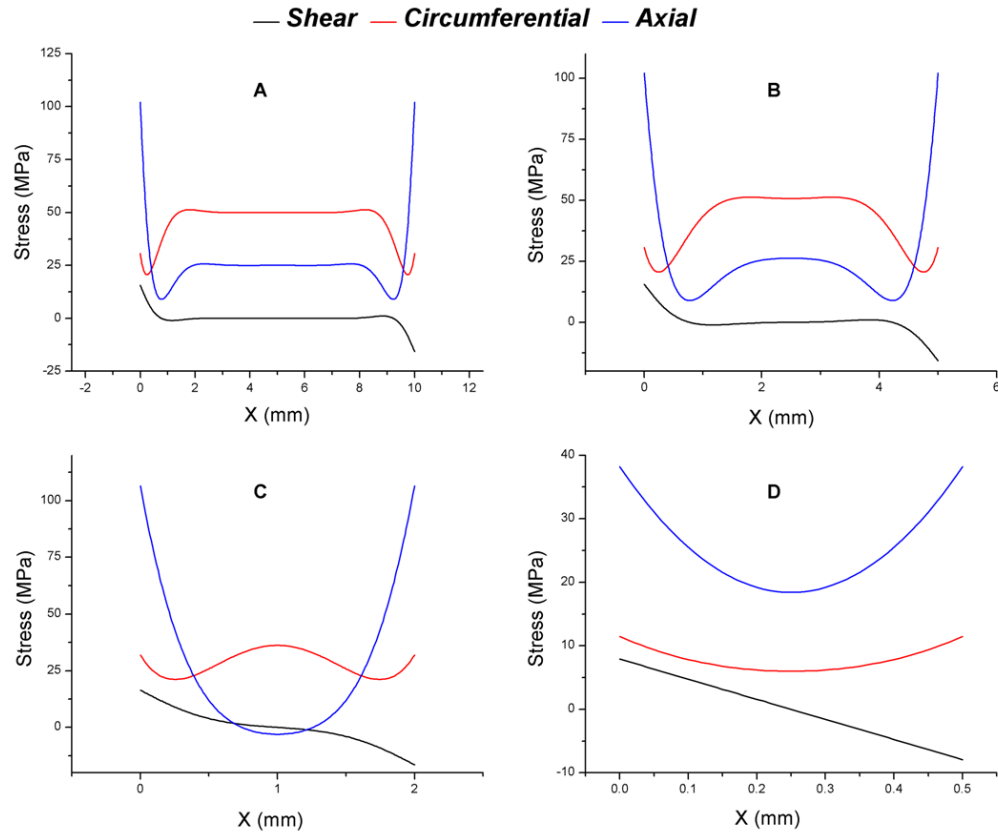


Figure 3-15: Stress components for various lengths of the annular cylinder: (A) 10 mm cylinder; (B) 5 mm cylinder; (C) 2 mm cylinder; and (D) 0.5 mm cylinder.

Comparing the four plots in Figure 3-15, we see that the stresses generated at the edges for the 0.5 mm long cylinder are much less than that of the longer cylinders. This is because the terms of the homogenous part of the deflection equation overlap and thus reduce the stresses generated due to the clamped edges. This result is similar to the stiffening effect of ring stiffeners for pipes carrying

fluids [25]. Hence, it can be concluded that, for a short shell, the stresses generated due to internal pressure are not large enough to be a concern for reliability.

Having undertaken the mechanical analysis, we introduce a thermal field (Figure 3-16) into the governing equation defined in equation 3.10.

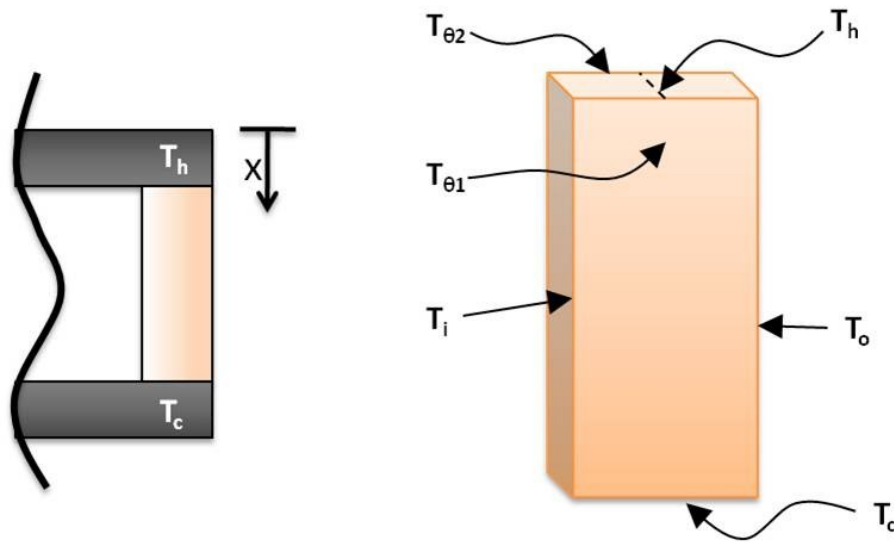


Figure 3-16: Differential element of the static sidewall with respective temperatures on the various surfaces.

With the assumption that $T_{\theta 1} = T_{\theta 2}$ and $T_i \sim T_o$, the linearly varying thermal field in the x-direction can be expressed as

$$T(x) = T_h - \left(\frac{T_h - T_c}{L} \right) x - T_{ref}. \quad (3.23)$$

Here, T_{ref} is the ambient temperature, T_h is the temperature of the hot surface, T_c is the temperature of the cold surface and L is the length of the sidewall. Using this

thermal distribution, a MATLAB code was used to evaluate the thermo-mechanical stresses of the short shell structure. Figure 3-17 shows a plot of the stresses of the inner and outer wall of the static sidewall of length 0.5 mm.

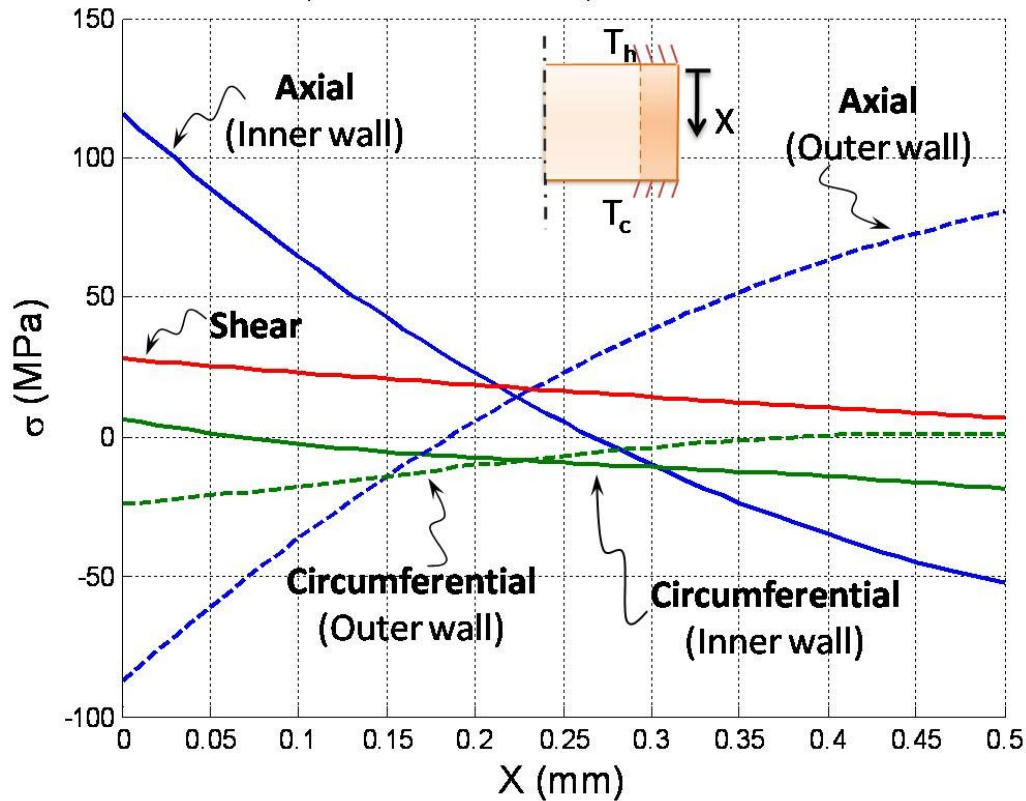


Figure 3-17: Variation of stress components along the length of the pressure vessel subjected to a thermal field ($T_h = 500^\circ\text{C}$, $T_c = 80^\circ\text{C}$ and $T_{ref} = 25^\circ\text{C}$) and an internal pressure of 5MPa. The solid lines represent stresses of the inner wall. The dashed lines represent stresses of the outer wall. Blue, green and red represent axial, circumferential and shear stresses respectively.

In Figure 3-17, the axial stress is tensile at the hot surface and compressive at the cold surface. This is because the high temperature causes thermal expansion near the hot edge hence generating tensile stresses. Based on the conditions imposed

on the sidewall, it can be seen that the thermomechanical stresses are below 120 MPa. This, in effect, shows that the hot end of the sidewall will expand and bulge compared to the cooler end.

The shell analysis enables us to identify the stress components of the 3D structure, and suggests that there is a stiffening mechanism that comes into effect for a short shell, and that the thermo-mechanical stresses have opposite signs for the two ends of the sidewall. The limitation of the shell analysis is that the shear strains are neglected. Moreover, the structure under consideration is not only short but also stubby, thus casting into doubt the thin shell assumption. The analysis also assumes clamped edges as boundary conditions, while in reality the sidewall rests on an elastic foundation.

3.3 Summary of analyses

In this chapter, simple analytical models were undertaken in order to capture thermal and mechanical aspects of the static sidewall. Table 3-1 highlights the conclusions obtained from these analyses.

Table 3-1: Summary of the analytical models undertaken in this chapter.

Model	Conclusions
1D heat transfer	<ul style="list-style-type: none"> ○ Oxides yield better device efficiencies. ○ Annular sidewall preferred as a means of reducing sectional area of the sidewall.
Euler-Bernoulli beam analysis	<ul style="list-style-type: none"> ○ There exists a minimum thickness for the annular sidewall, based on reliability considerations. ○ Si and SiC have a null design space for the sidewall.
2D plane strain elasticity	<ul style="list-style-type: none"> ○ Thermal stresses in the radial direction are negligible compared to the mechanical stresses.
3D shell theory	<ul style="list-style-type: none"> ○ Stiffening mechanism due to clamped edges of the short cylinder reduces the stress generated. ○ The stress is tensile at one end of the sidewall and compressive at the other end.

These analytical models provide valuable insight into the stresses experienced by the static sidewall and further refine material selection. However, they do not capture details that are excluded due to the assumptions made during the analyses. It is therefore necessary to conduct a detailed finite element analysis of the entire static structure to identify these details.

Chapter 4 – Finite element analysis

The static sidewall has thus far been studied using analytical models for thermal and mechanical behaviour, and these models have yielded key information regarding the design of the static structure. Staying true to the approach of undertaking analysis of increasing complexity, the static structure is next subjected to a coupled thermo-mechanical finite element analysis (FEA), whilst imposing the working conditions that have been obtained through heat transfer and force balance calculations. The commercially-available finite element software COMSOL is used to undertake this FEA of the static structure. Before proceeding with the detailed coupled thermo-mechanical analysis of the finite element model, the solver is used to make a quick check of the limitations of the shell theory for the sidewall.

Figure 4-1 shows the plot for the three principal stresses of the inner surface of the static sidewall, including the upper and lower plates (inset, top left), due to an internal pressure of 5 MPa. The principal stresses obtained from the finite element analysis show significant differences compared to that of the shell theory model (inset, top right). These differences arise due to the fact that the finite element model considers the sidewall to be bonded to elastic foundations (upper and lower plates), while the model implementing the shell theory assumes clamped edges. Hence, it can be seen that refining the boundary conditions significantly alters the behaviour of the stress field.

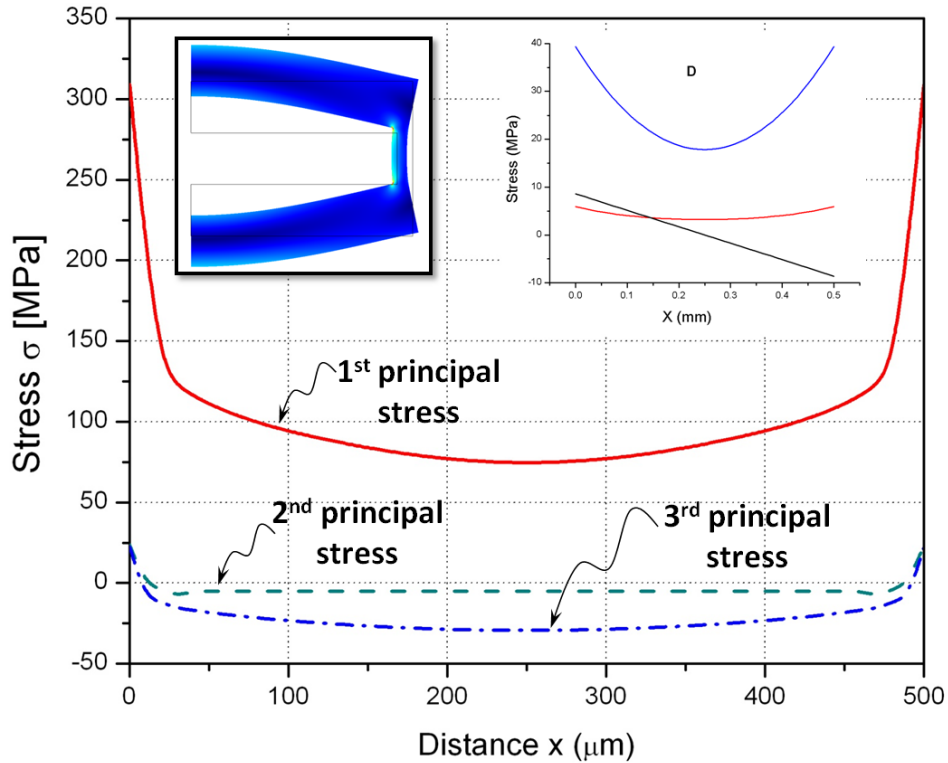


Figure 4-1: Principal stresses for static sidewall on elastic foundations obtained through FEA. The inset on the upper right hand corner shows the stresses obtained using shell theory for clamed edge boundary conditions. The inset on the upper left corner shows the result of the finite element analysis.

At this stage the boundary conditions are refined and a detailed finite element model of the proposed static structure consisting of a composite of fused silica and single-crystal silicon is conducted. This composite combines the low thermal conductivity of silica for the sidewalls, with ease of manufacturability of silicon for the top and bottom plates which contain the flow channels and pumps. As the static structure is rotationally symmetric about a central axis, a 2-dimensional axisymmetric FEA is undertaken. Figure 4-2 depicts the schematic of the axisymmetric model for which the initial FEA is conducted.

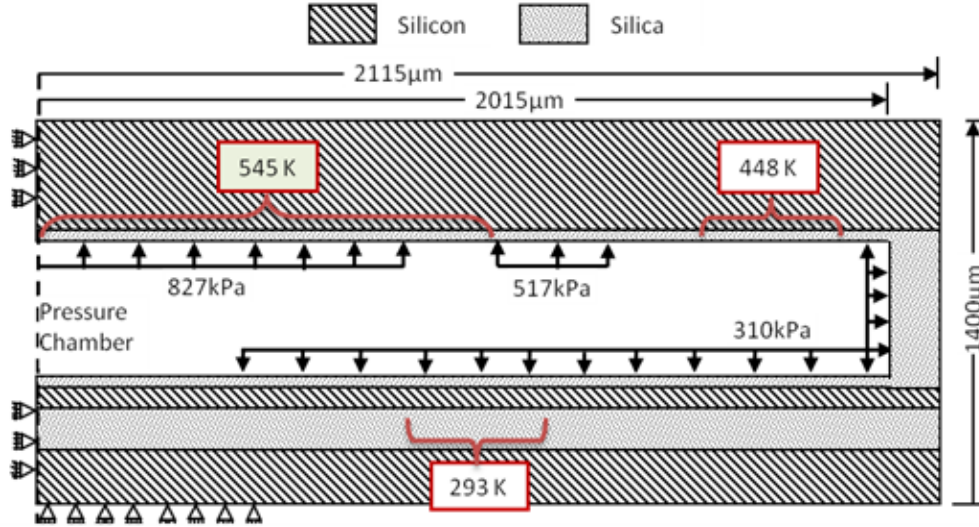


Figure 4-2: Axisymmetric schematic of the static structure modeled as a pressure vessel outlining structural dimensions, materials and the applied boundary conditions.

In Figure 4-2, the axis of symmetry is located on the left side of the schematic; hence, radial constraints are imposed on this surface. An axial constraint is placed on the bottom left hand side of the model in order to simulate the constraint imposed by the packaging of the device. The internal pressures and temperatures are obtained through heat transfer and force balance calculations, and were provided by Mr. M. Liamini (Université de Sherbrooke). The static sidewall and the inner surface of the upper and lower plates are comprised of silica in order to reduce the heat loss from the hot side to the cold side. Silicon makes up the portions which consist of intricate plumbing (not included in this finite element model) for the working fluid. The thickness of the bonded layers is 1400 μm and the radial thickness of the sidewall is taken to be 100 μm.

Temperature dependent properties of materials are used in this finite element model.

The results of the finite element analysis reveal two areas of concern. First, there is stress concentration at the edges where the static wall meets the upper and lower surfaces. Convergence of solutions at these locations was not achieved even after refining the meshed model to include 38150 elements. Second, there is considerable axial deflection (adjacent to the axis of symmetry) of the upper surface of the static structure due to the thermal expansion of the silicon layer. This may adversely affect the performance of the bearings. These concerns can be addressed through redesign of the static structure. One option is to employ fillets at the edges and to use a radial stiffener. The schematic of this option is depicted in Figure 4-3.

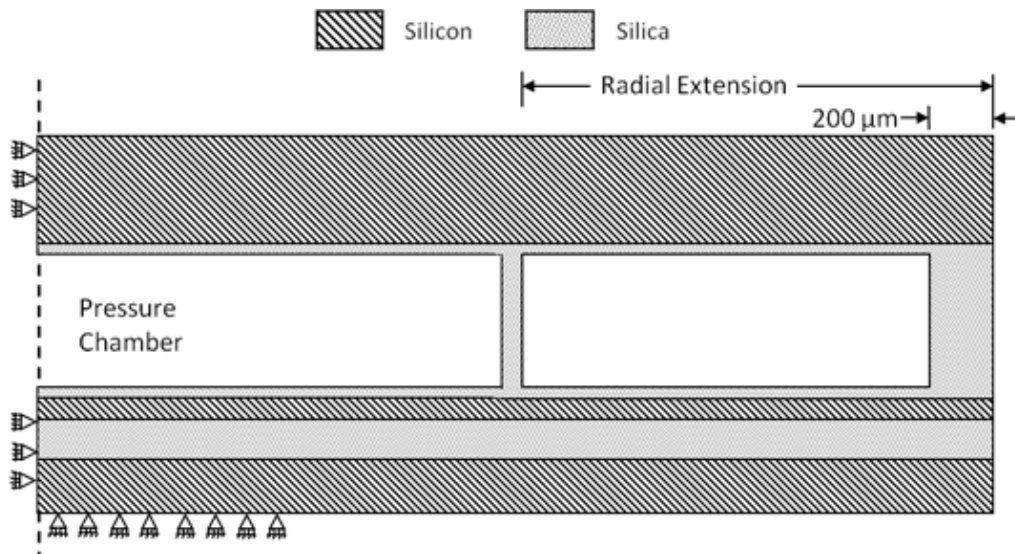


Figure 4-3: Modified schematic of the static structure including a radial extension outside the pressure chamber. Fillets are applied at all the corners where the inner and outer walls meet the upper and lower surfaces.

In this new design, the static structure consists of two cylindrical walls with the outer wall acting as the radial stiffener. Fillets are designed into the edges of both these walls. The variation of the maximum stress as a function of fillet radii is shown in Figure 4-4. The stresses can be significantly reduced by incorporating a fillet with a radius of $\sim 30 \mu\text{m}$. Also, the addition of the radial stiffener limits bowing of the upper surface and hence reduces the stresses in the inner wall. This effect is illustrated in Figure 4-5.

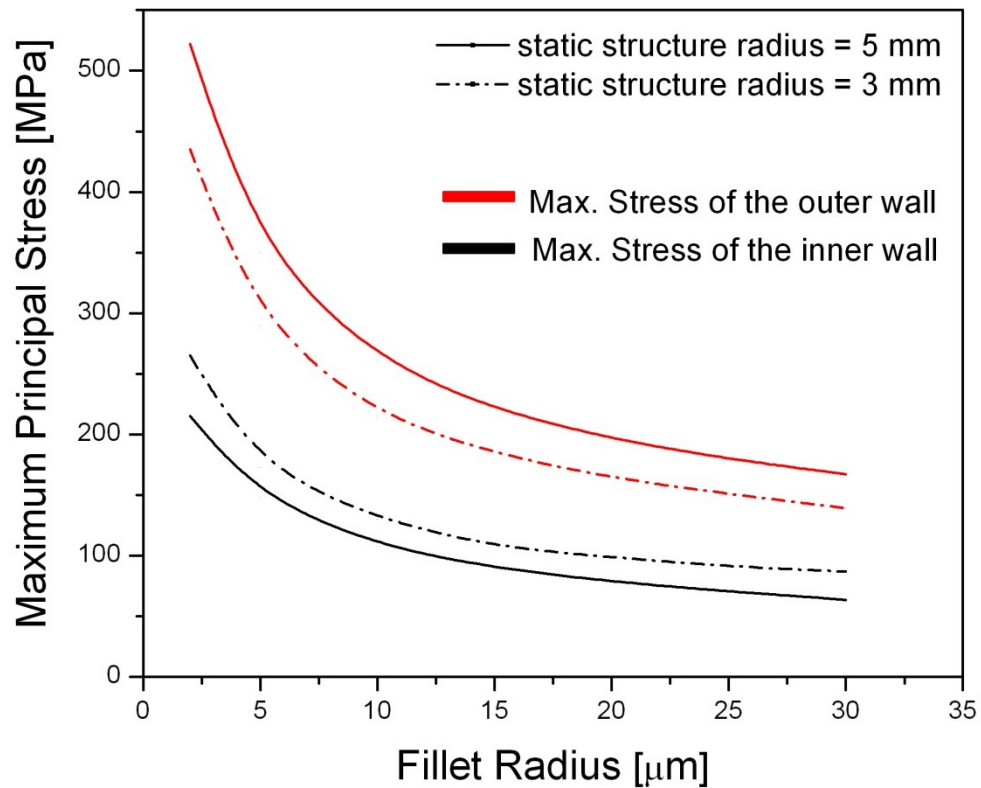


Figure 4-4: Variation of the maximum principle stress as a function of fillet radii obtained through a static finite element analysis. The solid lines represent the edge stresses of the inner and outer walls for a static structure of 5 mm radius. The dash-dot lines represent the change in edge stresses for a static structure of 3 mm.

Solution convergence tests were carried out before extracting results from post processing of the finite element analysis. Solution convergence for a model incorporating fillets with radius of 2 μm and 20 μm required 30913 elements and 10474 elements, respectively. An average of 35000 elements was used in each subsequent analysis, for fillet radii larger than 2 μm , to ensure convergence.

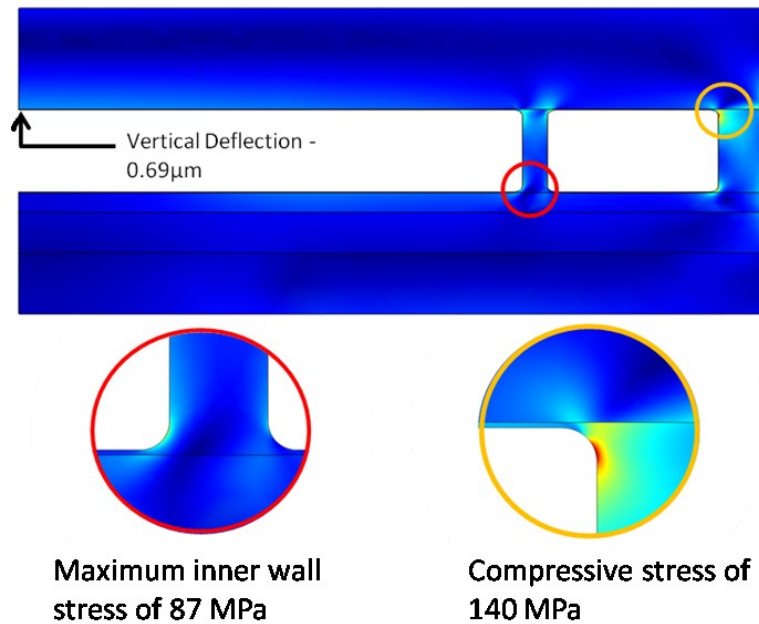


Figure 4-5: Results of the coupled thermo-mechanical finite element analysis with a static structure extension of 1 mm. The maximum stress for the outer wall is 140 MPa and is compressive. The location of the maximum deflection is indicated by the arrow and is approximately 0.69 μm .

The results of the new model reveal that: (i) the addition of stiffener at 1 mm from the static sidewall (3 mm radius from the centre) reduces the deflection of the upper surface by a factor of 2.5 from 1.74 μm to 0.69 μm ; and (ii) a fillet radius of 30 μm reduces the tensile edge stresses to 87 MPa, which is below the nominal flexural strength of silica.

4.1 Summary

In this Chapter, a coupled thermo-mechanical finite element analysis was undertaken to identify details not captured by the simplified analytical models. The FEA reveals that edge stresses and deflection are major concerns for the static structure composed of bonded layers. One option for addressing these concerns is to use edge fillets and a radial stiffener. A parametric finite element study shows that incorporating fillets with radius of 30 μm is sufficient to reduce the edge stresses below the flexural strength of silica. Also, placing 200 μm thick radial stiffener, at a distance of 1 mm from the static sidewall, reduces the deflection of the upper surface to acceptable levels. While these design changes are promising, this particular option entails within it micromachining challenges because it is not trivial to microfabricate fillets of 30 μm using silicon or silica.

Chapter 5 – Experimental Studies of Particle-Plate Impact

In the first generation Rankine micro-engine, the rotor was spun at 330,000 revolutions per minute (rpm) at room temperature on air bearings. Such high speeds are necessary for achieving acceptable efficiencies for the proposed second generation Rankine micro-engine. However, there are questions that remain regarding the dynamic reliability of the rotor spinning at almost half a million rpm at micrometer distances from the static sidewall. Thus far, there has been no study of the impact behaviour of millimetre-sized ceramic structures spinning at high speeds.

Ideally, one would conduct *in situ* reliability tests for the rotor within the micro-engine. The drawback to this method is that it yields no information regarding the failure mechanism of the rotor, since the rotor is enclosed within the engine architecture. A useful alternative is to conduct idealized tests to understand the failure mechanisms for brittle materials (representing the ceramic rotor) impacting on a brittle surface (representing the sidewall).

5.1 Background

A careful study by Andrews and Kim [28] of the response of ceramic particles impacting a hard TiB_2 target revealed the existence of a threshold velocity for damage for the particles. For impact at velocities less than the threshold value, the particle rebounded without damage. The value of the threshold velocity was found to depend on material properties and size of the particle. Finite element simulations further revealed that the peak tensile stress responsible for particle fragmentation depended not only on the impact velocity but also on the elastic properties of the target material [28]. Figure 5-1 shows the threshold velocity plots for alumina and silicon nitride particles; this graph is reproduced from the paper by Andrews and Kim [28].

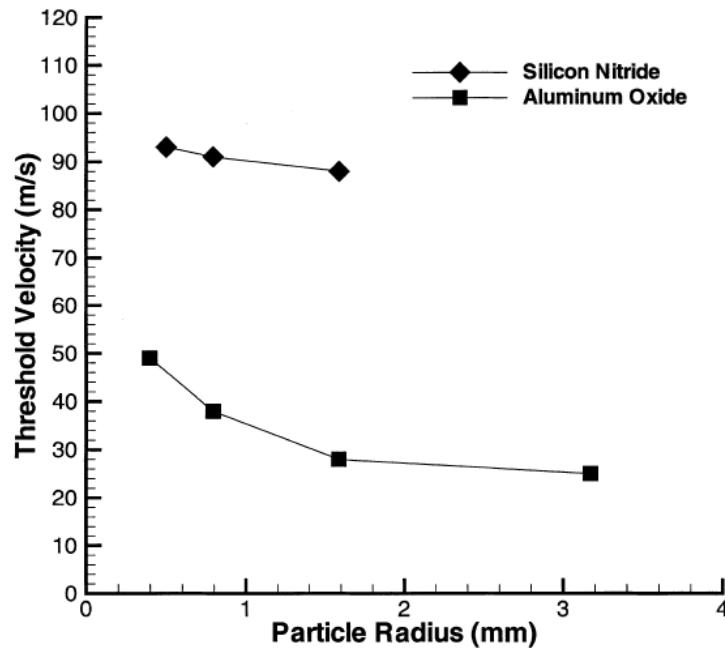


Figure 5-1: Threshold velocity plot for silicon nitride and alumina impacting on titanium diboride. (Source: E. W. Andrews and K. S. Kim (1998) *Mechanics of Materials*, vol 29: pp. 161-180).

Damage due to the impact of steel spheres on brittle surfaces (silicate, germanate, and borate glass) has also been investigated [29, 30]. Typically, Hertzian cone cracks are formed on the glass targets during the loading cycle, while lateral cracks form during the unloading cycle. There is considerable jetting of material for impact speeds in excess of 100 ms^{-1} . These results indicate that the properties of the target and those of the projectile are equally important in understanding the behaviour in a particle impact experiment.

5.2 Goal of the experiment

The goal of the experiments presented in this thesis is to identify the threshold velocities for brittle spherical projectiles impacting on brittle plates. The projectiles are 4 mm in diameter, which is comparable in size to the diameter of the rotor in the Rankine micro-engine.

5.3 Design of experiment

The design of the impact experiment revolves around two main factors: the range of velocities to be achieved, and the ability to measure these velocities. The maximum velocity chosen for this particle impact experiment is 100 ms^{-1} . This velocity is higher than the maximum tangential velocity of the rotor and the threshold velocity of silicon nitride [28]. This limit of 100 ms^{-1} is sufficiently low that a relatively inexpensive detection method can be used for measuring velocity. Hence, a digital camera (CASIO EX-F1), with a high speed movie recording

capability of 1200 frames per second, is chosen. A particle travelling at 100 ms^{-1} for a distance of 0.3 m will enable the high speed camera to capture at least 3 frames, which is sufficient to estimate the velocity of particle. Having identified the maximum velocity and the velocity detection method, the next step is to choose a method for propelling the projectile. A typical setup used in particle impact experiment is the gas gun. Figure 5-2 shows a schematic of the particle impact experiment setup used by Andrews and Kim [28].

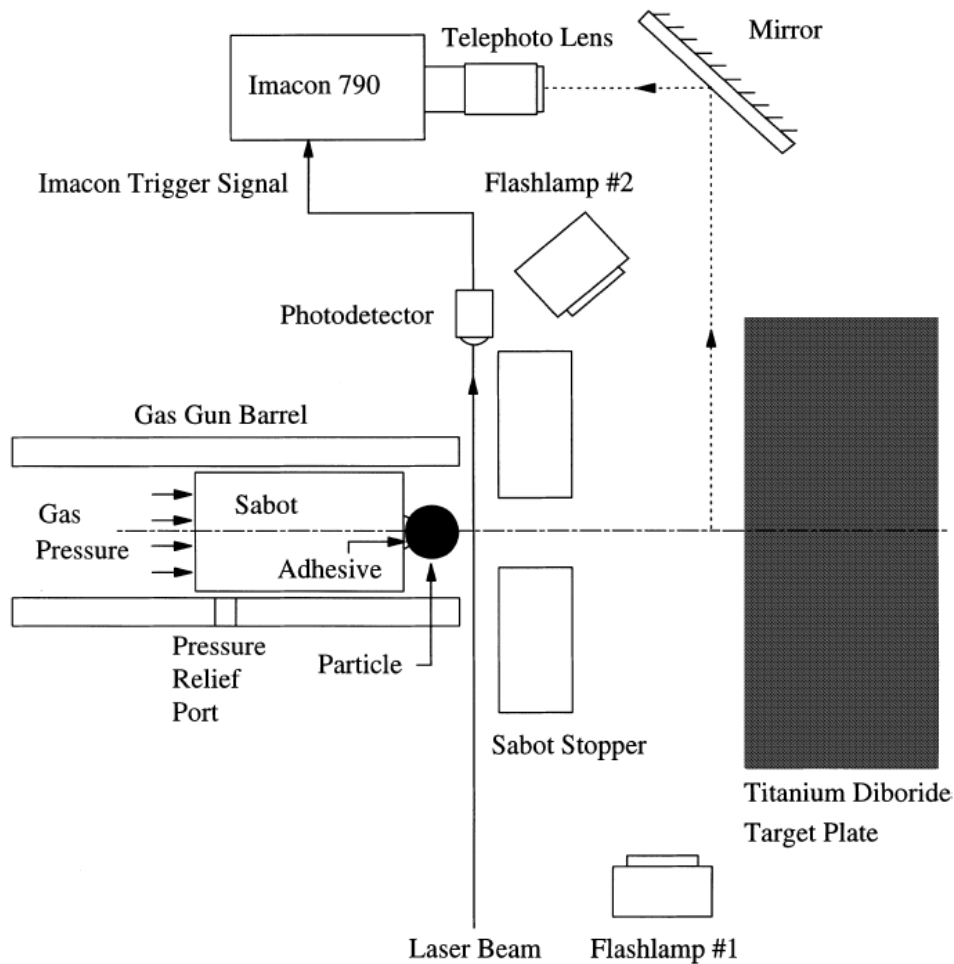


Figure 5-2: Schematic for particle impact experiment setup. (Source: E. W. Andrews and K. S. Kim (1998) *Mechanics of Materials* vol. 29, pp. 161-180).

This setup uses high pressure gas to propel a projectile through the bore of a gun barrel. In the case of smaller projectiles, a sabot is often used as a projectile carrier within the barrel. This arrangement achieves faster acceleration due to the gas pressure acting over a larger area. Owing to its simplicity in achieving high projectile speeds, a gas gun setup is chosen as the propellant system for our particle impact experiment. A vertical setup is designed (as opposed to a horizontal one) in order to create a more compact experiment setup and obviate the need for gluing the sample to the sabot.

The relevant parameters that dictate the velocity achieved at the end of the barrel are: (1) D_s – diameter of the Sabot; (2) P_o – pressure of the gas reservoir; (3) $W = mg$, where m is the mass of the sabot and the sample; (4) F – force exerted by P_o on the sabot; and (5) d – length of barrel.

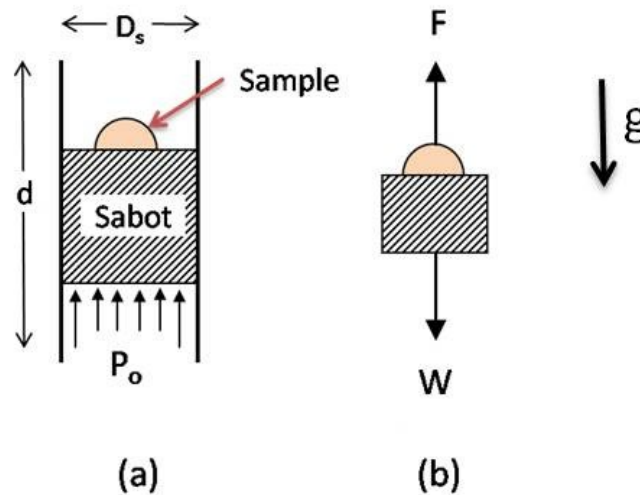


Figure 5-3: (a) Schematic of sample-sabot-barrel system (image not to scale). (b) Free body diagram of the sample and the sabot.

Using Newton's second law and kinematics, the relationship between velocity and the aforementioned parameters is given by

$$d = \left[\frac{V^2}{\left(\frac{2\pi P_o}{4m}\right) D_s^2 - 2g} \right], \quad (5.1)$$

where V is the exit velocity and g is the acceleration due to gravity. Equation (5.1) enables one to determine the length of the barrel and the diameter of the bore for given velocity, mass and gas pressure. With the maximum velocity limit set at 100 ms^{-1} , gas pressure of 7 bars (100 psig – chosen for commercially available compressors), and mass of 0.005 kg (sabot and sample), the design curve for the barrel length and bore diameter is determined and shown in Figure 5-4.

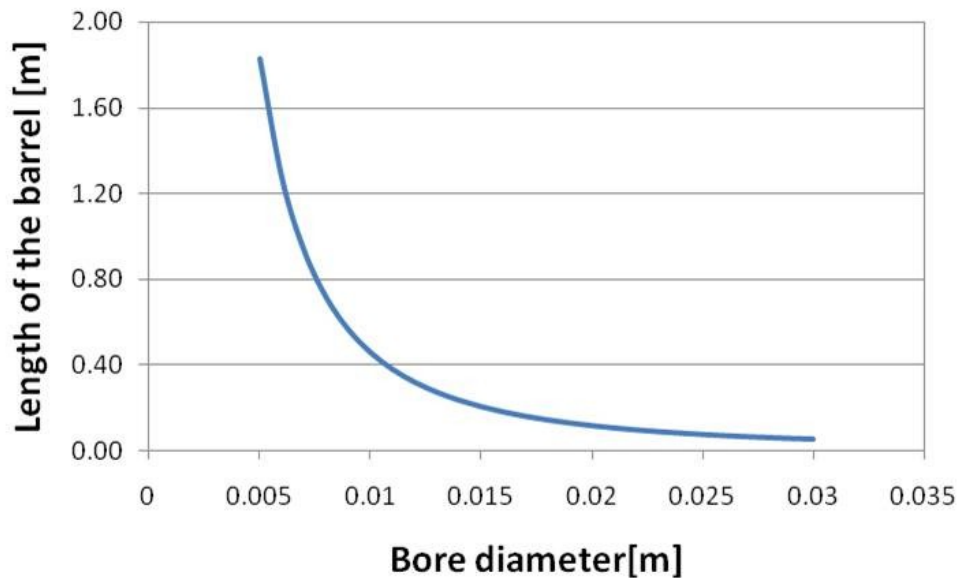


Figure 5-4: Design curve of the barrel length and bore diameter for the gun barrel for $V = 100 \text{ ms}^{-1}$, $P_o = 7 \text{ bars}$ and $m = 0.005 \text{ kg}$.

From Figure 5-4, it can be seen that a small bore requires a longer barrel. Since the sample is 4 mm in diameter, a bore diameter greater than twice the sample diameter is chosen, along with the corresponding barrel length.

At this stage, it is necessary to identify the major components needed to build the particle impact experiment setup. To start with, the necessary components for the experiment are identified and their functions defined.

Compressor: Commercially available DeWALT D55141 oil free portable compressor with a maximum tank pressure of 150 psi is chosen. This compressor allows the gas tank to be repeatedly filled with oil free air to pressures up to 150 psi.

Gas reservoir: A spare air scuba tank rated at 3000 psi and with a capacity of 13 cubic feet is chosen. The dead volume for the tank is at least 20 times the volume of the barrel in order to ensure that pressure drop during the firing process is minimal.

Solenoid valve: An Asco Redhat next generation solenoid valve is chosen. This is an electrically operated valve and acts as the trigger mechanism for the particle impact experiment. It is a two way valve which is normally closed, has an orifice diameter of half an inch and a pressure rating of 300 psi.

Ball valve: A ball valve is needed in order to close the air supply to the gas reservoir once the desired pressure has been achieved in the reservoir.

Gun barrel: A seamless stainless steel pipe with a smooth straight bore is chosen as the gun barrel. This pipe has an internal diameter of 0.406 inches (0.0103 m) and a length of 18 inches (0.4572 m). Hence this pipe falls within the vicinity of our design curve for the gun barrel.

Sabot: Sabots are machined from polycarbonate rods. Polycarbonate is chosen because of its light weight and impact resistance capabilities.

Protective casing: A casing made of 0.5 inch thick clear polycarbonate sheets is designed and built. This component encases the entire region within which the projectile is in flight thus preventing it from ricocheting off the target and causing injuries. The lid of the protective casing carries the target holder for this experiment.

High speed camera and ruler: The Casio EX-F1 is placed so that its field of view captures the entire flight of the projectile. The clear polycarbonate enables the digital camera to record a high speed movie of the particle in flight. A ruler is placed opposite to the camera so that distance travelled by the particle is captured in the high speed movie.

Support structure: A support structure constructed of 2x4 wood is constructed so as to contain all the components of the particle impact experiment.

A schematic of the piping system for the experiment setup is shown in Figure 5-5.

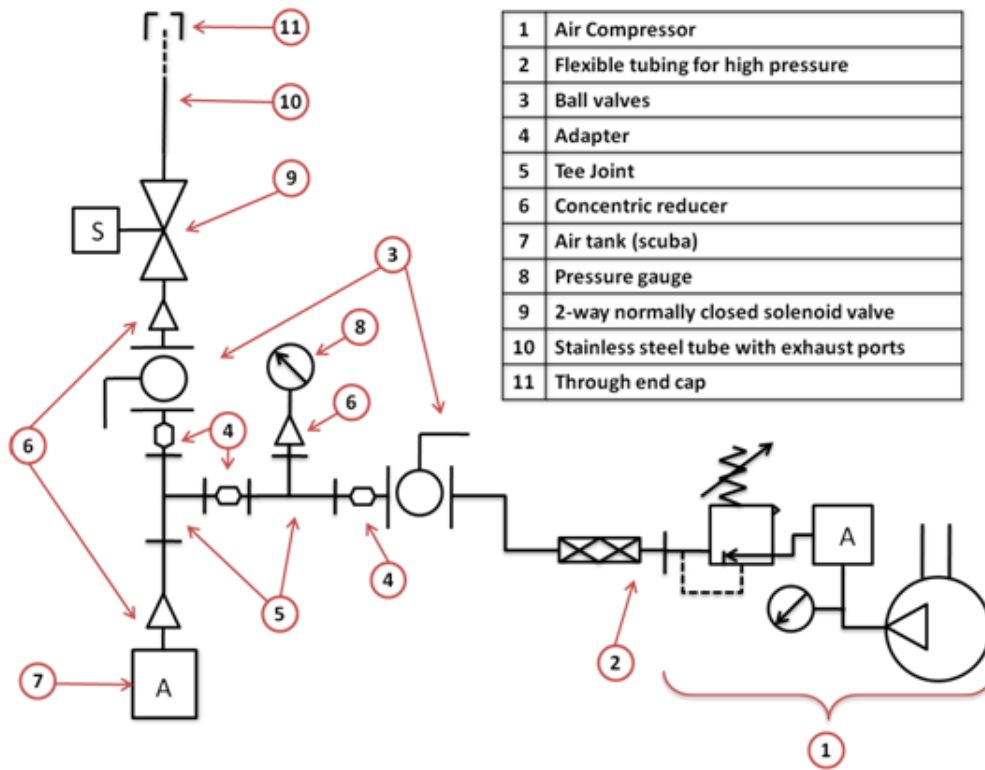


Figure 5-5: Schematic of the piping system for the gas gun system. The compressor includes a regulator, a pressure gauge and an air tank.

The piping system shown in Figure 5-5 depicts a simple gas gun design. Here the compressor (1) feeds air at a regulated pressure into the air tank (7). A pressure gauge (8) records the equilibrated pressure between the air tank and the compressor. The ball valve (3) to the right of the pressure gauge is then closed, hence decoupling the compressor from the rest of the setup. At this stage the air tank is considered to be charged. The ball valve (3) to the left of the pressure gauge is opened and the pressure reading from the pressure gauge is recorded. Finally the solenoid valve (9), which is normally closed, is energized (opened) thus allowing the pressurized air within the tank to escape through the stainless

steel pipe (10). The sabot which is placed within the pipe (barrel) is propelled through it and is stopped by the end cap (11) while the pressurized air escapes through the exhaust port. Figure 5-6 shows a photograph of the particle impact experiment setup.

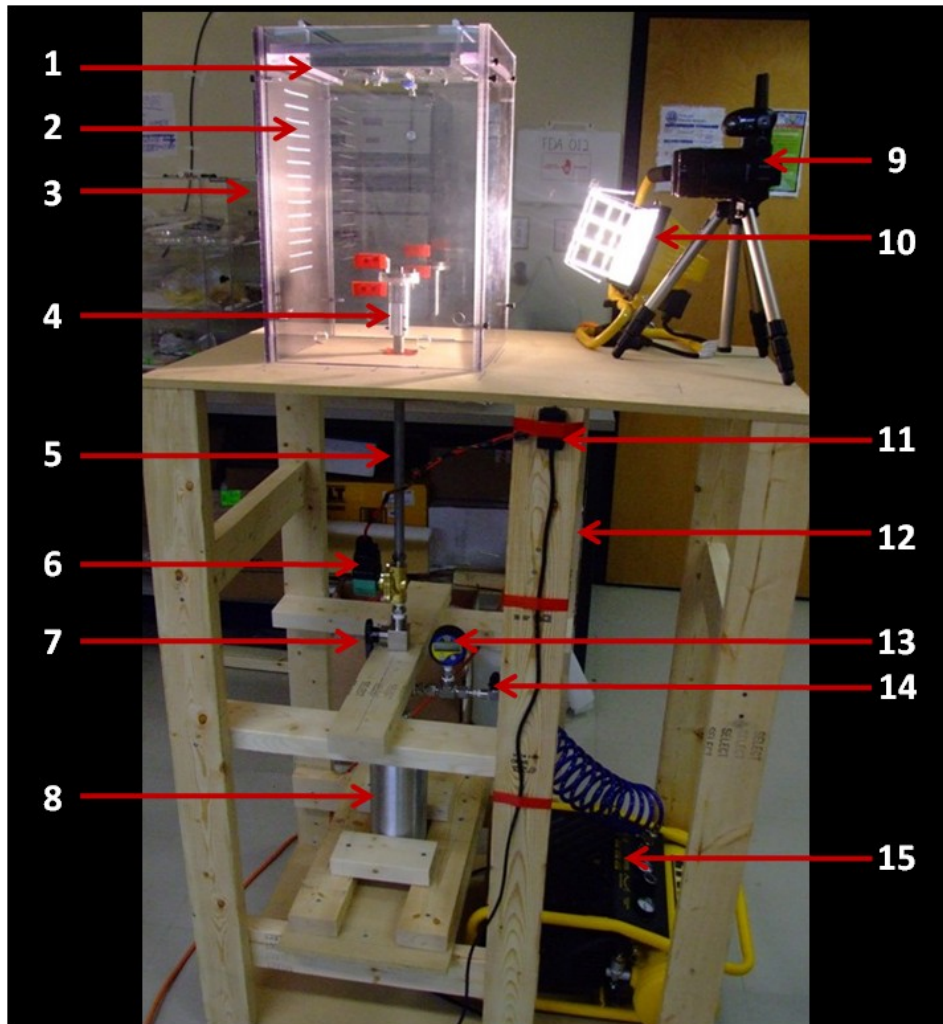


Figure 5-6: Particle impact experiment setup. (1) Target holder (2) Ruler (3) Protective casing (4) End cap (5) Barrel (6) Solenoid valve (7) Ball valve (8) Air tank (9) High speed camera (10) Lamp (11) Trigger switch (12) Support structure (13) Pressure gauge (14) Ball valve (15) Air compressor.

5.4 Velocity estimation and verification

The experiment setup is designed to achieve particles being shot at a target at varying velocities. Measuring these velocities is of critical importance to the goal of the particle impact experiment. To begin with, a high speed camera records the flight of the particle as it leaves the barrel and proceeds towards the target across a ruled background. The apparent distance travelled by the particle over the ruled background is converted to the real distance that the particle travels along its trajectory. From the high speed video, frames are selected which yield best estimates for the apparent distances travelled over the ruled background. The average velocity is then estimated using the time between the frames and the real distance that the particle covers. Figure 5-7 shows two sets of frames of the high speed recording for air tank pressures of 5 psi and 50 psi.

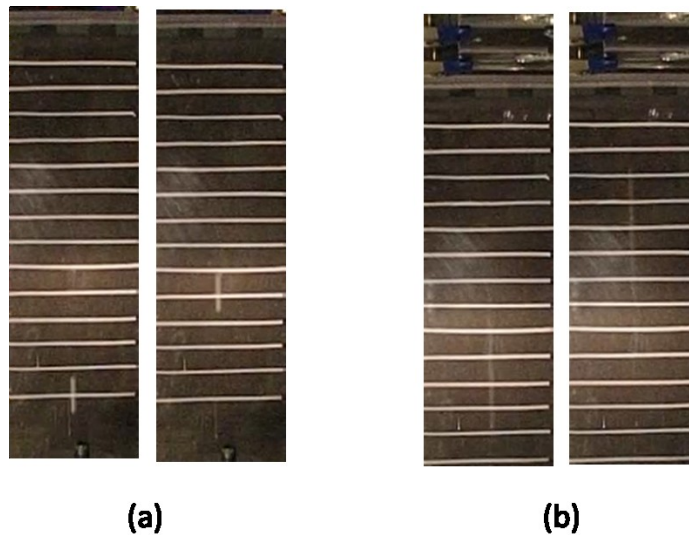


Figure 5-7: (a) Two frames of the particle trajectory for a 5psi (34kPa) air tank pressure. The frames are 0.0025 seconds apart. (b) Extracted frames for a 50psi (344kPa) air tank pressure. The frames are 0.000833 seconds apart. Due to lack of luminous intensity, the particles appear as a blur, more so for higher velocities.

Similarly, the average velocities of the particle for different tank pressures have been estimated. Using equation (5.1), the velocities for these pressures are calculated. The plot in Figure 5-8 shows two sets of experiments for speed verification.

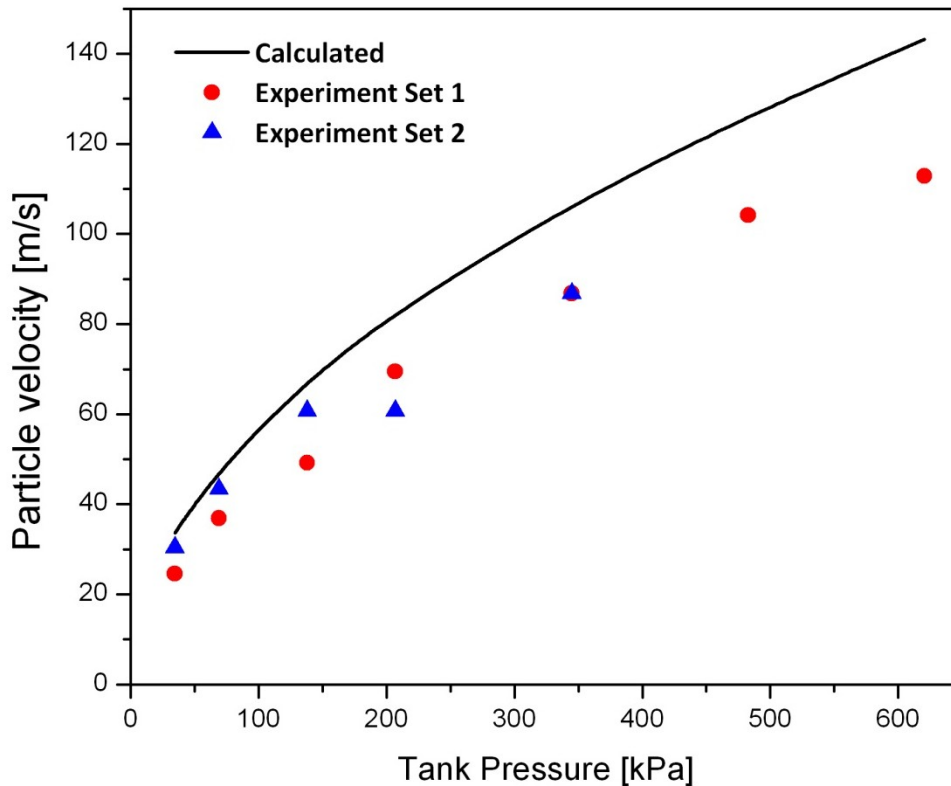


Figure 5-8: The solid black line represents the calculated velocity of the particle based on equation 5.1 where the parameters d , D_s , m and P_o are known. The red and the blue points represent the estimated velocities of the particle based on the extracted frames from the movie of the particle trajectory.

From Figure 5-8, it can be seen that the velocities obtained via the high speed camera system are less than the calculated velocities for varying tank pressures. This is expected as the calculated velocities omit frictional losses and

sabot condition. It can also be seen from the plot that at higher pressures, the differences between the velocities of the experiment and the calculations increase. This can also be attributed to the frictional losses in the barrel which increase as the velocity of the sabot increases.

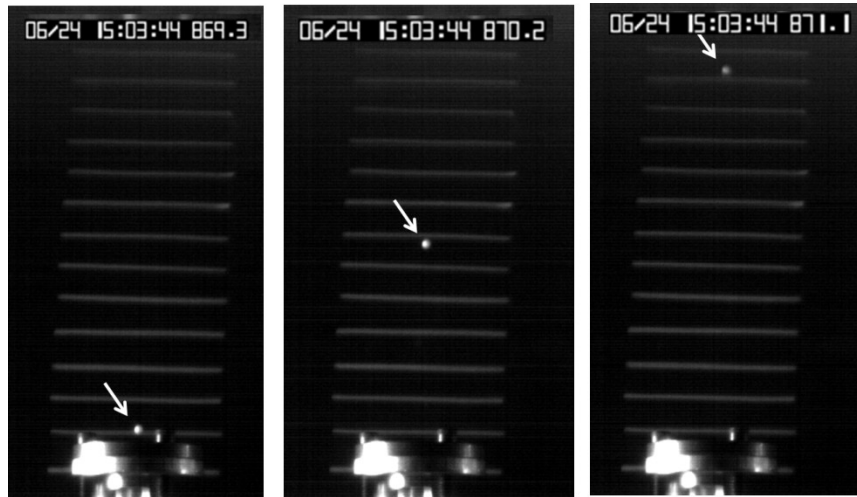


Figure 5-9: Particle fired with an air tank pressure of 70 psi (483kPa). The white arrow indicated the location of the spherical particle in three consecutive frames. Image source: High Speed video camera model MS50K with high illuminance light source – Optikon Corporation.

Figure 5-9 shows the location of the particle as it travels across the ruled background. These images were taken using a high speed camera (model MS50K) as part of a demonstration by a representative from Optikon Corporation. The software included with the system determined the velocity of the particle to be 95.21 m/s. On the other hand, using the ruled background, the first two frames yielded an estimated velocity of 96.47 m/s. Hence, the error in using the ruled background for velocity estimation is limited to below 1.5% based on the above comparison.

5.5 Particle impact experiment: Test materials and results

The goals of the particle impact experiment are to identify threshold velocities of zirconia and alumina and to assess the damage that may take place on borosilicate glass and alumina targets. Table 5-1 lists the materials together with their sizes and shapes used in this experiment.

Table 5-1: Materials, shapes and sizes used in the particle impact experiment.

	Materials	Shape and Size
Projectile	Zirconia	Sphere – $\varnothing 3.97$ mm
	Alumina	Sphere – $\varnothing 3.175$ mm
Target	Borosilicate glass	Plate – 101.6 mm x 101.6 mm x 6.35 mm
	Alumina	Disc – $\varnothing 76.2$ mm x 3.175 mm

The zirconia balls were obtained from Ortech Advanced Ceramics while the glass and the alumina balls and discs were obtained from McMaster-Carr. The manufacturer of the alumina samples is CoorsTek and the samples are composed of 99.9% alumina. Table 5-2 lists some of the properties of the test materials at room temperature obtained from the manufacturers and from the paper by Andrews and Kim [28].

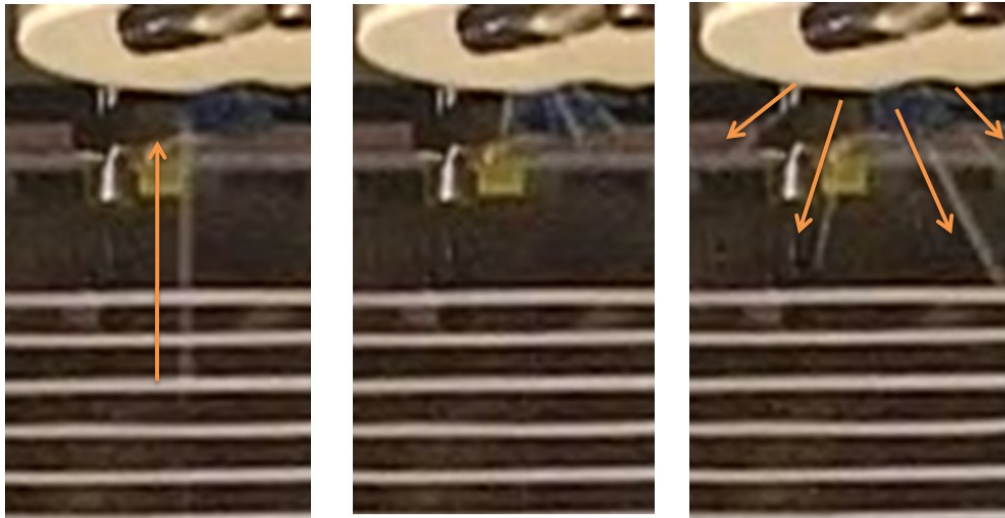
Table 5-2: Selected properties of test materials.

Materials	Zirconia	Alumina	Borosilicate (glass)
Density (g/cm ³)	6.02	3.9	2.23
Young's Modulus (GPa)	208	380	64
Poisson's ratio	0.23-0.31	0.25	-
Fracture toughness (MPa m ^{1/2})	13	4-5	-
Compressive strength (MPa)	1850	2000	-
Vickers Hardness (kg/mm ²)	1300	1900	-

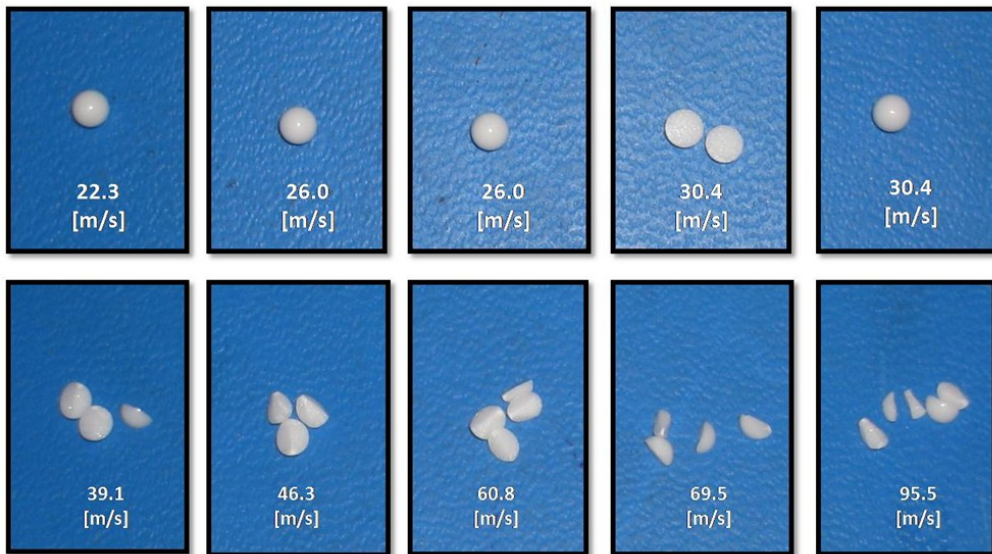
The list of impact tests are as follows: (1) alumina ball on alumina disc (for threshold velocity verification), (2) zirconia ball on borosilicate plate, and (3) zirconia ball on alumina disc.

5.5.1 Results – Alumina spheres on alumina disc

Ten impact tests were carried out using alumina balls of Ø3.175 mm at different tank pressures (different velocities). Each test was undertaken with a new alumina ball. Figure 5-10 (a) shows three consecutive frames capturing the splitting up of the alumina ball. Figure 5-10 (b) shows the conditions of the alumina balls after impact at different velocities.



(a)



(b)

Figure 5-10: (a) Three consecutive frames of capturing the fragmentation of the alumina ball. Arrow in the first frame shows the direction of the ball. Arrows in the third frame shows the direction of the ball fragments (b) Post impact remains of the alumina balls (impact velocities indicated).

The alumina target suffered little to no damage hence the same disc was used in all the ten experiments. The angle between the fragments (third frame of Figure 5-10a) increased with higher impact velocities. At lower velocities, the number of

fragments decreased. At 39.1 m/s, the alumina ball split into three pieces while at 30.4 m/s it splits into two pieces. This is consistent with the fragmentation behaviour as reported by Andrews and Kim [28]. Using the results of the above experiment, we can identify the threshold velocity for the alumina ball of $\varnothing 3.175$ mm. Figure 5-11 shows a plot of experiment results.

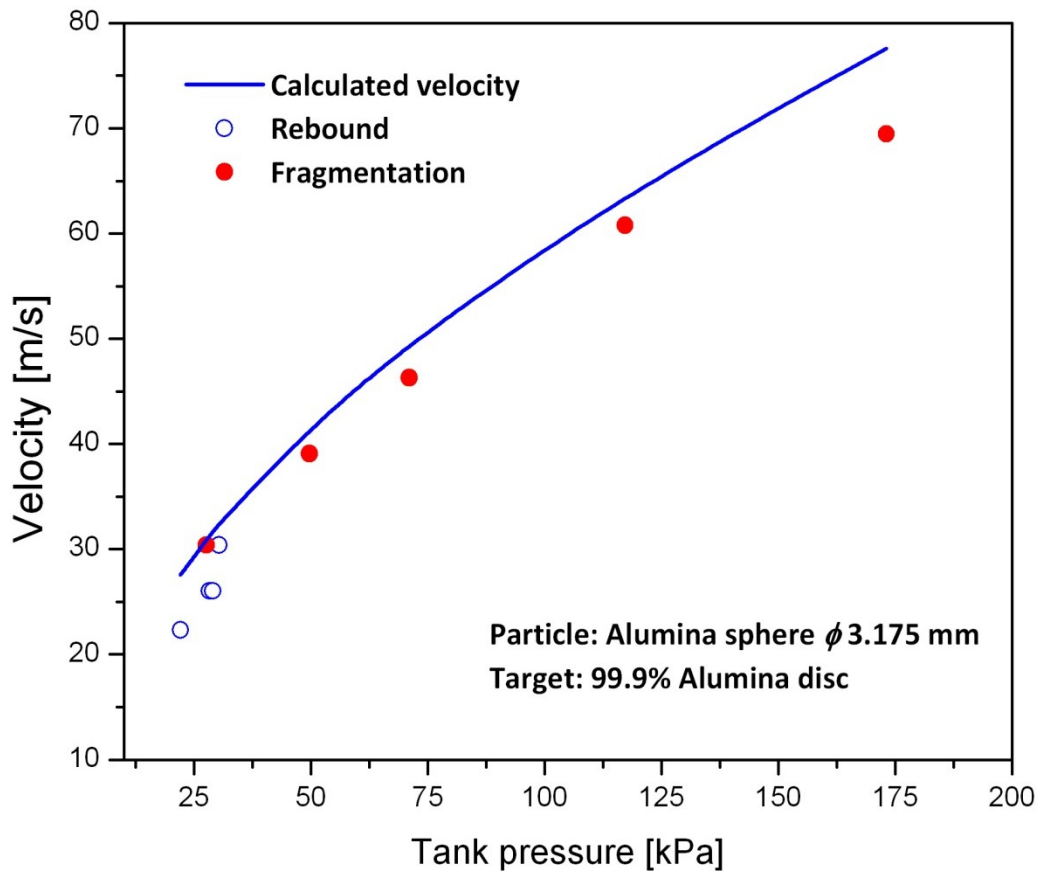


Figure 5-11: Calculated and experimental velocities of the alumina ball impacting on alumina target. Filled circles indicate fragmentation of the alumina particle, while hollow circles indicate rebound.

The threshold velocity for the alumina particle impacting an alumina target is approximately 30 m/s. Andrews and Kim report a comparable threshold velocity

of the same sized alumina particle at 25 m/s [28]. However, this discrepancy can also be attributed to the difference in the elastic properties of the target materials. Andrews and Kim used titanium diboride (elastic modulus - 575 GPa) instead of alumina (elastic modulus - 380 GPa) as the target. Targets with higher modulus represent shorter contact time during impact, hence higher peak tensile stresses within the particle, which leads to fragmentation at lower velocities.

5.5.2 Results – Zirconia spheres on borosilicate glass

Impact experiments were carried out with zirconia spheres shot at borosilicate targets at varying speeds. In each case, there was no visible damage of the zirconia particle. The borosilicate glass on the other hand suffered considerable damage, even at low speeds. Figure 5-12 shows pictures of the damage taking place on the borosilicate glass. Figure 5-13 shows two SEM images of the damage to borosilicate glass at 23 m/s and at 69 m/s.

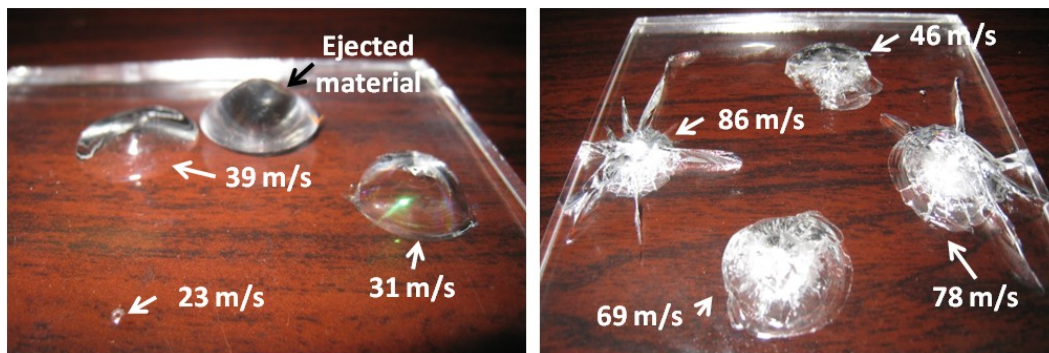


Figure 5-12: Damage of borosilicate glass at various impact speeds with zirconia spheres. Cone cracks appear at lower velocities. At 39 m/s, a conical piece is removed from the target. Frosted regions and lateral cracks appear at higher impact velocities.

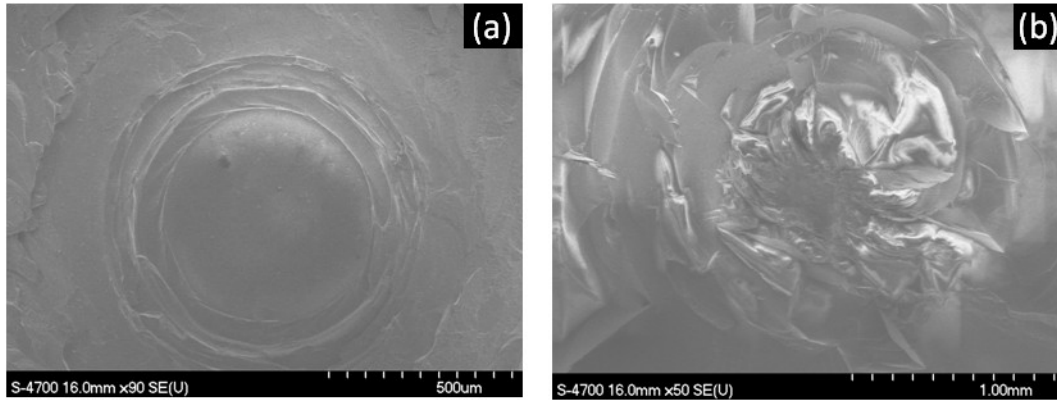


Figure 5-13: Scanning electron micrograph of borosilicate glass after impact at (a) 23 m/s, and at (b) 69 m/s. Images show material removed from the impacted region.

The impact tests show that zirconia sphere is capable of withstanding impact velocities up to 104 m/s if target material is borosilicate glass.

5.5.3 Results – Zirconia spheres on alumina

In this test, the zirconia particles were fired at alumina discs at different velocities. The results of zirconia impacting on alumina are represented in Figure 5-14.

5-16 shows two SEM images of the zirconia pieces for an impact that resulted in fragmentation.

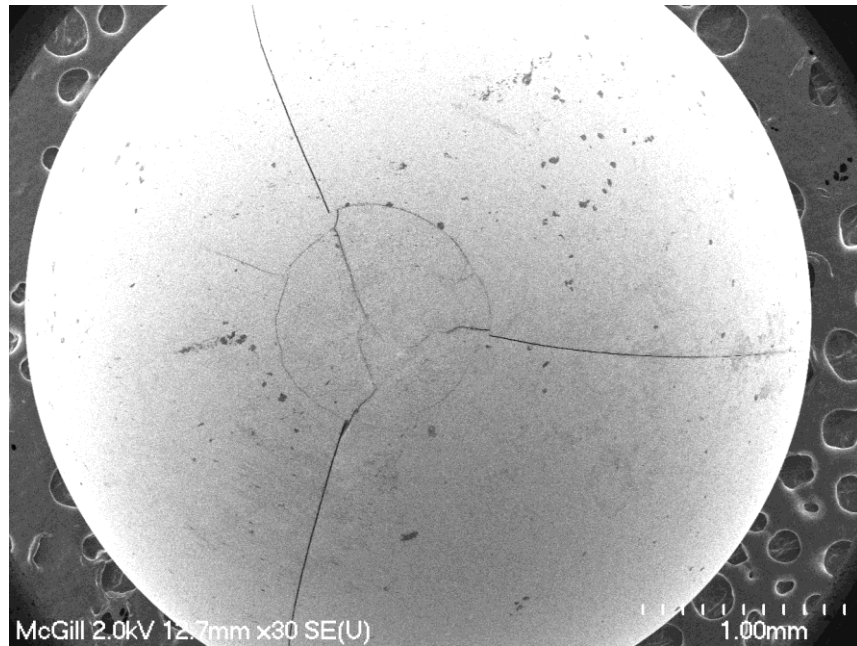


Figure 5-15: Scanning electron micrograph of a zirconia ball after impact at 69.5 m/s. A ring crack forms in the contact zone together with lateral cracks extending across the ball surface.

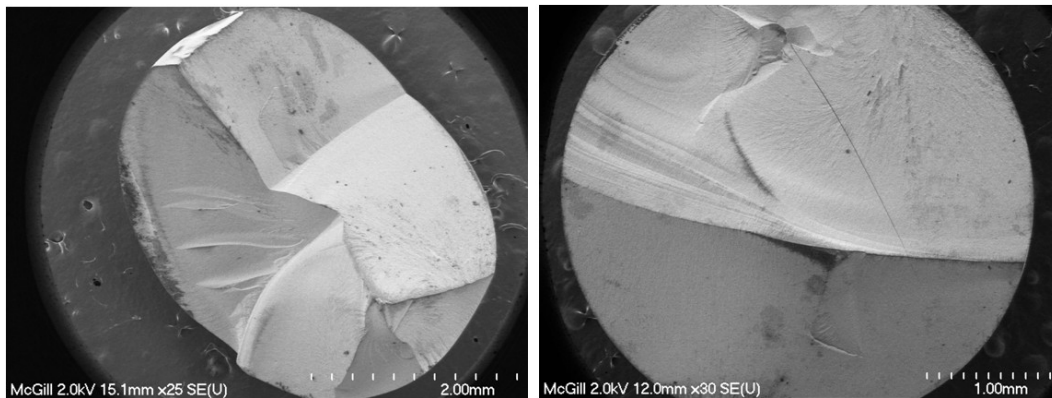


Figure 5-16: Split pieces of a zirconia ball formed through lateral separation mode.

5.6 Summary

In an effort to answer questions pertaining to the dynamic reliability of the rotor, a particle impact experiment was designed and performed with the goal of identifying threshold velocities for the materials of interest. The experiment was conducted for zirconia and alumina particles impacting on borosilicate glass and alumina targets. The threshold velocity for alumina projectile on alumina target was identified and found to be approximately 30 m/s. There was also minimal damage to the alumina target. Next, zirconia balls were shot at borosilicate glass plates. Threshold velocity for zirconia was not reached for this material pair as zirconia remained intact at velocities up to 104 m/s. The glass target on the other hand suffered surface damage even at low velocity impacts.

In the third set of tests, zirconia balls were shot at an alumina target. Here a velocity region was identified in which the zirconia balls either rebounded intact with surface cracks or underwent fragmentation. Several tests reveal signs of two threshold velocity limits for a given material pair. The first limit demarcates particle rebound from particle rebound with cracks. The second limit demarcates rebound with cracks from particle fragmentation. Further tests are needed to establish the validity of this statement.

Finally, these idealized impact tests pave the way for a design map to be developed for material combinations for the rotor and the static sidewall of the Rankine micro-engine.

Chapter 6 – Conclusions and Future Work

The work presented in this thesis provides the foundation for the design of a pressure vessel type structure for a Rankine micro-engine. This foundation includes an approach to material and shape selection for the components of the Rankine micro-engine. This is followed by laying the ground work to study the impact behaviour for the materials of interest for the engine components.

To begin with, the Ashby approach was implemented to select a promising group of materials and it was realized that a trade-off exists between performance, reliability and manufacturability of the engine components. The selected materials can be classed primarily into oxides (zirconia and silica), alloys (titanium and nickel cobalt) and ceramics (silicon and silicon carbide).

Simple analytical models of increasing complexity of the static sidewall enabled a quantitative selection of the materials of interest and yielded zirconia, silica and titanium alloy as the ideal materials. The analytical models also highlighted the need for a detailed finite element analysis in order to incorporate the coupled thermo-mechanical effects within the static structure. The finite element analysis pinpointed two areas of concern, namely, stress concentration and deflection. These were addressed by incorporating fillets into the edges and including a radial stiffener to the static structure. Parametric finite element analyses of the new geometry revealed that fillets with a radius of 30 μm are

needed to mitigate the edge stresses. The analyses also show that a stiffener placed 1 mm from the static sidewall helps reduce deflection of the upper surface.

Having identified materials, shape and design of the static structure, the focus of this thesis shifts towards rotor reliability. Motivated by the lack of information on high speed impact of millimetre-sized ceramic rotors, and by the inability to assess the failure mechanism of the rotor during engine operation, an idealized impact experiment was carried out. The goal of the experiment was to establish threshold velocities for the materials of interest. These experiments serve as a first step in addressing the dynamic reliability of the rotor in the event of a high speed impact during engine operation.

Three sets of experiments were carried out. The first set involved shooting alumina balls of $\text{Ø}3.175$ mm on to an alumina target. Threshold velocity of approximately 30 m/s was established for the projectile/target material pair. Next, zirconia balls of $\text{Ø}3.97$ mm was shot at borosilicate plates. Here, the threshold velocity for zirconia particle was not reached for velocities up to 104 m/s. However, the glass underwent damage even at low velocity impacts. The final set of tests involved zirconia balls of $\text{Ø}3.97$ mm shot at alumina target. Two post impact scenarios were observed. First, the zirconia balls rebounded intact for velocities up to 65 m/s. Second, the zirconia balls either underwent fragmentation or rebounded with surface cracks for velocities higher than 65 m/s. Hence a threshold velocity region of 65-70 m/s can be attributed to this material pair.

The future work for this ongoing project can be divided into two parts. The first part will be to refine the finite element model to include the rotor and to take into account the fluidic conditions within the enclosed pressure chamber on the performance and reliability of the static structure.

The second part will be to conduct further impact tests with various material pairs in order to develop a design map that will enable appropriate combination of materials to be selected for the rotor and the static sidewalls of the Rankine micro-engine. Improvements to the impact experiment setup can be made by: (1) upgrading the velocity measurement system through the purchase of a high speed camera such as the MS50K (Optikon Corp), (2) modifying the support structure so as to prevent misalignment of the barrel relative to the target plate, and (3) redesigning the end cap of the barrel so as to incorporate shock absorbing rubber washers.

References

- [1] A. H. Epstein, "Millimeter-Scale, Micro-Electro-Mechanical Systems Gas Turbine Engines," *Journal of Engineering Gas Turbines and Power*, vol. 126, pp. 205-226, 2004.
- [2] D. Lindley, "The energy should always work twice," *Nature*, vol. 458, pp. 138-141, 2009.
- [3] J. H. Lang, *Multi-Wafer Rotating MEMS Machines*, Springer, 2009.
- [4] A. H. Epstein, S. D. Senturia, O. Al-Midani, G. Anathasuresh, A. Ayon, K. Breuer, K. -S. Chen, F. E. Ehrich, E. Esteve, L. Fréchette, G. Gauba, R. Ghodssi, C. Groshenry, S. Jacobson, J. L. Kerrebrock, J. H. Lang, C. -C. Lin, A. London, J. Lopata, A. Mehra, J. O. Mur Miranda, S. Nagle, D. J. Orr, E. Piekos, M.A. Schmidt, G. Shirley, S. M. Spearing, C. S. Tan, Y. -S. Tseng and I. A. Waitz, "Micro-Heat Engines, Gas Turbines, and Rocket Engines" *AIAA Journal*, pp. 97-1773, 1997.
- [5] C. Lee and L. G. Fréchette, "Demonstration and Characterization of a Multi-Stage Silicon Microturbine," in *Proceedings of IMECE 2005-81435, Orlando, Florida*, November 5-11, 2005.
- [6] C. Lee, M. Liamini and L. G. Fréchette, "Design, Fabrication, and Characterization of a Microturbopump for a Rankine Cycle Micro Power Generator," in *Proceedings of Solid State Sensor, Actuator, and Microsystem Workshop, Hilton Head Island, SC*, June 4-8, 2006.
- [7] P. Beauchesne-Martel and L. G. Fréchette, "Numerical Analysis of Sub-Millimeter-Scale Microturbomachinery Aerothermodynamics," in *Proceeding of IMECE 2008-68190*, Boston, Massachusetts, October 31 – November 6, 2008.
- [8] L. G. Fréchette, C. Lee, S. Arslan and Y. -C. Liu, "Design of a Microfabricated Rankine Cycle Steam Turbine for Power Generation," in *Proceedings of IMECE 2003-42082, Washington, D.C.* November 16-21, 2003.
- [9] M. F. Ashby, *Materials Selection in Mechanical Design*, Boston, Elsevier, 2005.
- [10] V. T. Srikar and S. M. Spearing, "Materials Selection in Micromechanical Design: An Application of the Ashby Approach," *Journal of Microelectromechanical Systems*, vol. 12, pp. 3-10, Feb. 2003.

- [11] S. M. Spearing, "Material issues in microelectromechanical systems (MEMS)," *Acta Materialia*, vol. 48, pp. 179-196, 2000.
- [12] W. D. Kingery, J. Francl, R. L. Colbe and T. Vasilos, "Thermal Conductivity: X, Data for Several Pure Oxide Materials Corrected to Zero Porosity Part II," *Journal of American Ceramic Society*, vol. 37, pp. 107-110, 1954.
- [13] C. Y. Ho, R. W. Powell and P. E. Liley, "Thermal Conductivity of the Elements," *Journal of Physical and Chemical Reference Data*, vol. 1, pp. 279-421, 1972.
- [14] M. J. Assael, K. Gialou, K. Kakosimos and I. Metaxa, "Thermal Conductivity of Reference Solid Materials," *International Journal of Thermophysics*, vol. 25.
- [15] Z. A. Musaeva and V. E. Peletskii, "Experimental Investigation of the Thermal Conductivity of VT6 Alloy," *Journal of High Temperature*, vol. 40, pp. 838-842, 2002.
- [16] W. C. O'Mara, R. B. Herring and L. P. Hunt, *Handbook of Semiconductor Silicon Technology*, William Andrew Publishing/Noyes, 1990.
- [17] A. Marsh and D. A. Bell, "High Temperature Flexural Strength of Engineering Ceramics," *International Journal of High Technology Ceramics*, vol. 4, pp. 26-273, 1988.
- [18] D. C. Jia, Y. Zhou and T. C. Lei, "Ambient and Elevated Temperature Mechanical Properties of Hot-Pressed Fused Silica Matrix Composite," *Journal of European Ceramic Society*, vol. 23, pp. 801-808, 2003.
- [19] S. R. Choi and J. A. Salem, "Ultra Fast Fracture Strength of Advanced Ceramics at Elevated Temperatures," *Journal of Material Science and Engineering*, vol. A242, pp. 129-136, 1998.
- [20] S. J. Kalita, S. Qiu and S. Verma, "A Quantitative Study of the Calcination and Sintering of Nanocrystalline Titanium Dioxide and its Flexural Strength Properties," *Journal of Material Chemistry and Physics*, vol. 109, pp. 392-398, 2008.
- [21] H. L. Chao and T. E. Parker, "Tensile Fracture Strength of ST Cut Quartz," in *Proceedings of the 37th Annual Frequency Control Symposium*, Philadelphia, PA, USA, June 1-3, 1983.
- [22] W. N. Sharpe, G. M. Beheim, L. J. Evans, N. N. Nemeth and O. M. Jadaan, "Fracture Strength of Single-Crystal Silicon Carbide Microspecimens at 24°C and 1000°C," *Journal of Microelectromechanical Systems*, vol. 17, pp. 244-254, 2008.

- [23] S. Nakao, T. Ando, M. Shikida and K. Sato, "Changes in Mechanical Properties of Micron-sized Single-Crystal-Silicon film at High Temperature," in *13th International Conference on Solid-State Sensors, Actuators and Microsystems, Seoul, Korea*.
- [24] A. P. Boresi and R. J. Schmidt, *Advanced Mechanics of Materials*, John Wiley & Sons, Inc., 2003.
- [25] P. L. Gould, *Analysis of Shells and Plates*, Springer-Verlag New York Inc. 1988.
- [26] M. H. Sadd, *Elasticity, Theory, Applications and Numerics*, Elsevier Butterworth-Heinemann, 2005.
- [27] S. Timoshenko and J. N. Goodier, *Theory of Elasticity*, McGraw-Hill, USA. 1951.
- [28] E. W. Andrews and K. S. Kim, "Threshold Conditions for Dynamic Fragmentation of Ceramic Particles," *Mechanics of Materials*, vol. 29, pp. 161-180, 1998.
- [29] M. M. Chaudhri and C. R. Kurkjian, "Impact of Small Steel Spheres on the Surfaces of Normal and Anomalous Glasses," *Journal of American Ceramic Society*, vol. 69, pp. 404-410, 1986.
- [30] A. Ball and H. W. McKenzie, "On the Low Velocity Impact Behaviour of Glass Plates," *Journal de Physique IV*, vol. 4, 1994.